Characteristics of a horizontal square jet interacting with the free surface

Godwin F. K. Tay, Mohammad S. Rahman, and Mark F. Tachie
Department of Mechanical Engineering, University of Manitoba, Winnipeg, Manitoba, Canada R3T 5V6
(Received 18 October 2016; published 23 June 2017)

The characteristics of a horizontal submerged square jet interacting with the free surface are investigated experimentally. A particle image velocimetry system is used to measure the mean flow and turbulent characteristics in the vertical symmetry plane of the jet at a Reynolds number of approximately 5500. It is shown that the effect of the free surface is to cancel the turbulent-nonturbulent interface and reduce the mean spanwise vorticity, Reynolds shear stress, and jet spreading rate in the upper shear layer in comparison to those measured in the lower shear layer. The results indicate that lowering of the jet offset height ratio increases the confinement effect of the free surface. Stronger confinement reduces the maximum mean streamwise velocity decay rate and mean surface velocity defect in the interaction region. The results also indicate a dramatic reduction in surface-normal turbulence intensity in the interaction region due to the damping effect of the free surface on the surface-normal velocity fluctuations. The decay of the surface-normal turbulence intensity near the free surface produces commensurate reductions in the surface-normal velocity fluctuation autocorrelation in the upper shear layer while enhancing the streamwise velocity fluctuation autocorrelation. The damping effect of the free surface on the surface-normal velocity fluctuations is found to be connected to the redistribution of the turbulent kinetic energy from the surface-normal velocity fluctuations to the streamwise velocity fluctuations.

DOI: 10.1103/PhysRevFluids.2.064607

I. INTRODUCTION

The physics of submerged turbulent jets issuing near the free surface is of great importance in a number of geophysical and technological applications. Examples include submerged jets discharged from river dams, pollutant mixing in rivers, and the interaction between the submerged wake of a surface ship and the free surface. In these flows, also known as surface-attaching jets, the interaction between the jet and the free surface results in a more complex jet structure compared to their deep or free counterparts. For example, the anisotropy of turbulence generated by the kinematic free-surface boundary condition may give rise to surface currents. The presence of surface currents, accompanied oftentimes by the deformation of the free surface, can lead to more complicated flow physics and boundary conditions at the free surface compared to a solid wall.

The prototypical turbulent free jets have been studied in considerable detail both experimentally and numerically in the past and a fairly large volume of literature has now evolved on the subject (see, e.g., Refs. [1–6]). A comprehensive review of previous experiments on axisymmetric and noncircular jets can be found in Refs. [7,8] and previous numerical investigations on incompressible turbulent jets are summarized by Dewan *et al.* [9]. It is widely accepted that the near-field structure of a turbulent jet is dominated by large-scale coherent vortex rings generated by the Kelvin-Helmholtz instability of the shear layer [4,6]. Since the early works of Roshko [10], coherent structures in jets have been studied with great interest because of their dynamical significance in mixing applications. Therefore, understanding their dynamics and topology is a necessary ingredient in the development of efficient methodologies for enhancing the jet mixing and spreading characteristics.

Although turbulent free jets issuing from circular and noncircular nozzles have been extensively investigated, confined jets such as those issuing from a square nozzle are very limited. Previous experimental observations [6,11] indicate that the entrainment and spreading characteristics of square free jets are considerably different from those in circular nozzles, due largely to the dynamics

of coherent structures. Generally speaking, turbulent jets issuing from noncircular nozzles have been shown to entrain more ambient fluid and spread more quickly than their circular counterparts because the circumferential vortices from noncircular nozzles undergo more rapid deformation compared to those from circular nozzles. Additionally, the presence of sharp corners at the edge of the jet is considered to induce a nonuniform deformation of the circumferential rings, leading to the axis switching of the jet cross section [6,11].

Most previous investigations on surface-attaching jets have been conducted using single-point measurement methods such as Pitot-static tubes (e.g., [12,13]), hot films (e.g., [14,15]), and the laser Doppler velocimeter (e.g., [16–18]). Due to the restrictions of pointwise measurement techniques, the results from these studies are limited to single-point quantities such as the mean velocity, turbulent intensities, and Reynolds stresses. Rajaratnam and Humphries [12] reported mean streamwise velocity measurements for three types of surface jets: a plane surface jet and surface jets issuing from circular and rectangular nozzles mounted flush with the free surface. They found that the spreading rates of the surface jets are considerably lower than those in their free counterparts. For the jets at high Froude numbers, a characteristic decrease was observed in the mean velocity in the vicinity of the free surface. Mean velocity and momentum flux measurements were reported by Ead and Rajaratnam [13] for a plane surface jet at varying offset heights relative to the channel bed. The presence of confinement (reservoir wall and channel bed) was found to cause flow reversal and a decrease in the momentum flux by amounts that increase with increasing offset height ratio. Swean *et al.* [14] obtained single-component hot-film measurements of the mean streamwise velocity and turbulence intensity in a plane surface jet inside a channel of limited depth. They found that the main effects of the jet confinement were to decrease the jet spreading rate but increase the mean streamwise velocity decay rate. Madnia and Bernal [15] used a single-component hot film to measure the mean velocity and turbulence intensity profiles in a round jet issuing at various offset height ratios $h/D = 1, 1.5, 2.5$, and 3.5, where h is the offset height measured from the free surface to the center of the nozzle and D is the nozzle diameter. They suggested a model of the free surface as a symmetry plane with the submerged jet merging with its twin or image jet above the free surface at sufficiently low Froude number.

Using a three-component laser Doppler velocimetry (LDV), Anthony and Willmarth [16] obtained mean velocity and turbulence intensity measurements in a submerged round jet with offset height ratio $h/D = 2$. They reported a decrease in the surface-normal turbulence intensity accompanied by an increase in the streamwise and spanwise turbulence intensities. The reduction in surface-normal turbulence intensity was attributed to the redistribution of the turbulent kinetic energy from the surface-normal velocity fluctuations to the streamwise and spanwise velocity fluctuations. Their spanwise measurements indicated that beneath a clean free surface, there exists a shallow outward spreading layer of fluid (called the surface current) moving predominantly downstream, with spanwise extent much greater than the jet flow beneath it. In another investigation, with similar nozzle geometry and offset height ratio, Walker *et al.* [17] used a three-component LDV to evaluate the influence of the Reynolds number and Froude number on the jet–free-surface interaction. It was found that the damping effect of the free surface on the surface-normal fluctuations is independent of Reynolds number but decreases with increasing Froude number and downstream distance. It was demonstrated that the turbulent kinetic energy redistribution mechanism and the outward spreading of the surface current are the direct results of the interaction of the streamwise component of the instantaneous vorticity vector with the free surface.

In the present investigation, a high-resolution particle image velocimetry (PIV) method was used to characterize the influence of nozzle offset height ratio on the structure of a square jet issuing in the vicinity of a free surface. Only a few previous investigations applied the PIV measurement technique to study the flow fields of turbulent surface-attaching jets. These include the recent investigations by Rahman and Tachie [19] and Tian *et al.* [20] and the earlier work by Tsunoda *et al.* [21], all of which presented the one-dimensional profiles of the mean velocity and higher-order statistics. Among the main contributions of the present work are a detailed discussion of the impact of the jet–free-surface interaction on the two-point statistical correlations, mean flow, and turbulence scaling at the free

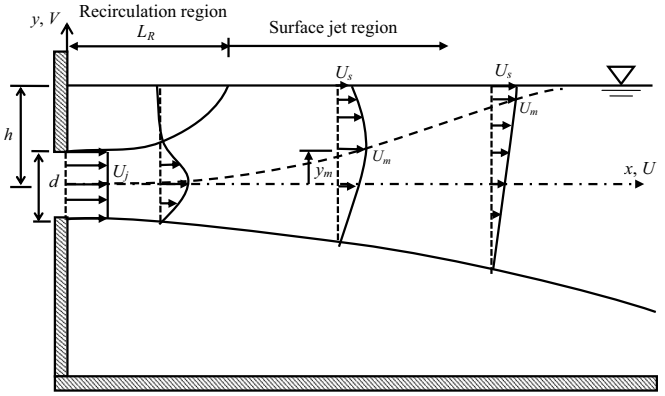

FIG. 1. Test section.

surface, as well as the relative contributions of the various turbulence events using joint probability density function and weighted joint probability density function analyses.

II. EXPERIMENTAL SETUP AND METHODOLOGY

The experiments were carried out in an open water channel of length 2500 mm and cross-section dimensions $200 \times 200\,\text{mm}^2$. The channel was fabricated from clear acrylic plates to provide easy optical access. The flow in the channel was driven by a centrifugal pump through a series of flow conditioning units that include a perforated metal plate, a hexagonal honeycomb, mesh screens, and a 6.5:1 converging section. The resulting fine-scale flow then exited through the square nozzle mounted flush with the inlet section of the channel. The nozzle was constructed from 3-mm-thick acrylic glass plates and has cross-section dimensions $10 \times 10\,\text{mm}^2$ with sharp edges. Figure 1 shows a schematic of the vertical symmetry plane through the jet. As indicated in the figure, the origin is located at the center of the nozzle exit; x and y are the streamwise and surface-normal directions, respectively, U and V are the mean streamwise and surface-normal velocity components, respectively, U_j represents the maximum mean streamwise velocity at the exit along the centerline of the jet, U_m is the local maximum mean streamwise velocity, y_m is the surface normal location of U_m relative to the nozzle centerline, and U_s is the mean streamwise velocity at the free surface. The jet centerline passing through the locations of U_m, divides the jet into two regions, above and below the centerline, hereinafter referred to as the upper and lower shear layers, respectively.

Experiments on the jet were conducted at four offset height ratios of $h/d = 1,2,3$, and 4, where d is the width of the nozzle. All experiments were run at a jet exit velocity of approximately 0.55 m/s, corresponding to Reynolds number of approximately 5500 based on the jet exit velocity and nozzle width. The Froude numbers based on the jet exit velocity and offset height are $\text{Fr} \approx 1.76, 1.24, 1.01$, and 0.88, respectively.

A PIV system was used to conduct detailed velocity measurements in the vertical jet symmetry plane. The flow was seeded with 10-μm silver-coated hollow glass spheres. The specific gravity of the seeding particles was 1.4. The values of the estimated settling velocity and response time were 2.18×10^{-5}m/s and 7.78×10^{-6}s, respectively, which ensured that the particles followed the flow faithfully. An Nd:YAG double-pulsed laser with a maximum energy of 120 mJ per pulse at 532-nm wavelength was used to illuminate the seeding particles. The thickness of the laser sheet was maintained at about 1 mm, which reduced the number of defocused particles within the measurement planes. The reflected beam from the seeding particles was captured by a 12-bit f-number-2.8 charge-coupled device camera with a resolution of $2048 \times 2048\,\text{pixels}^2$ and a pixel pitch of 7.4 μm. The particle image diameter was estimated as 2.4, which is in good agreement with 2.0, recommended by Raffel *et al.* [22] to minimize peak locking. In order to increase the streamwise

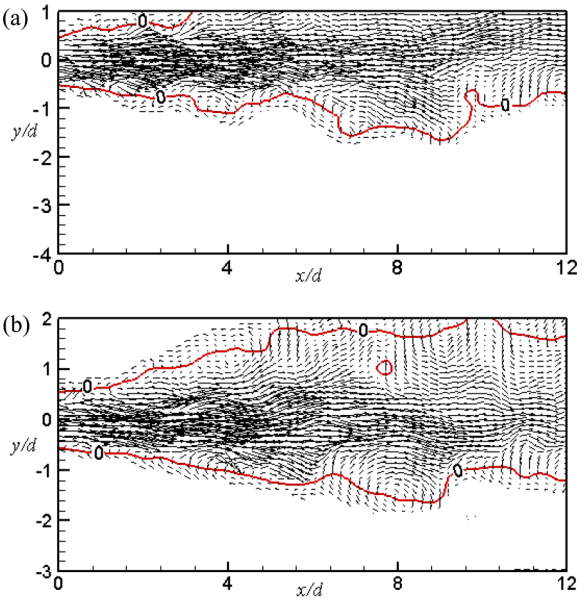

FIG. 2. Instantaneous velocity vector maps obtained by a Galilean decomposition of the flow fields for (a) $h/d = 1$ and (b) $h/d = 4$. Solid lines denote the isocontours of the normalized fluctuation level $(U_{\text{inst}} - 0.15U_j)/U_j$.

extent of the flow field, measurements were made in two contiguous planes: $0 \leqslant x/d \leqslant 12.5$ and $12.5 \leqslant x/d \leqslant 25$. The field of view (FOV) of the camera in each plane was set to approximately $135.0 \times 135.0\,\text{mm}^2$. Based on preliminary statistical convergence tests, an ensemble size of 5000 images was found to be sufficient for the flow statistics to converge. The data were postprocessed using the adaptive correlation option of DynamicStudio. The interrogation area (IA) size of the correlation was set to $32 \times 32\,\text{pixels}^2$ with 50% overlap in both the x and y directions. The adaptive correlation algorithm used a multipass fast Fourier transform with a one-dimensional Gaussian peak-fitting function to determine the average particle displacement within the interrogation area. Steps were taken during the image acquisition to ensure that the maximum particle displacement was less than one-quarter of the IA size. From the processed images, the mean velocities and higher-order turbulence statistics were calculated and used to characterize the jet–free-surface interaction. Using the measurement uncertainty methodology [23], the uncertainties in the mean velocity, turbulence intensities, and Reynolds shear stress at the 95% confidence level were estimated to be $\pm 3\%, \pm 7\%$, and $\pm 10\%$, respectively.

III. RESULTS AND DISCUSSION

A. Instantaneous velocity fields

Typical instantaneous vector fields in the vertical symmetry plane of the jet are shown in Fig. 2 for the offset height ratios $h/d = 1$ and 4. The vectors were plotted over the streamwise range of $0 \leqslant x/d \leqslant 12.5$, which includes the near-field and attachment regions of the jet. A Galilean decomposition was applied, with a constant convection velocity of $0.15U_j$ subtracted from each instantaneous velocity field (U_{inst}). Superimposed on the vectors are the corrugated contours of the normalized fluctuation level $(U_{\text{inst}} - 0.15U_j)/U_j$. The decomposition reveals groups of counterclockwise rotating (retrograde) spanwise vortex cores at the edge of the upper shear layer and clockwise rotating (prograde) spanwise vortex cores at the edge of the lower shear layer. The spanwise vortex cores are consistent with previous flow visualizations [6,11] that indicate a rolling up of the square vortex sheets shed from the exit into ringlike vortices under the Kelvin-Helmholtz instability

mechanism. The vortex rings induce braidlike structures, indicated by the darker areas in the region $0 < x/d < 7$, propagating in the downstream direction. The corrugated contour lines passing through the centers of the spanwise vortex cores correspond to the turbulent-nonturbulent interface of the jet. Such an interface is characteristic of all turbulent shear layers and has been investigated widely in the past for turbulent jets using dye markers and planar laser-induced fluorescence [24,25]. The mechanics of mixing and fluid entrainment by the jet is often evaluated in terms of the small-scale nibbling and large-scale engulfment motions at the turbulent-nonturbulent interface [25–27]. In the plots, the small-scale nibbling motions can be considered as the counterrotating spanwise vortex cores at the turbulent-nonturbulent interface, while the large-scale engulfment motions correspond to the fluid regions between successive vortex cores. The results in Fig. 2(a) indicate that the effect of confinement by the free surface is to nullify the turbulent-nonturbulent interface and suppress the vortical structures responsible for mixing and entrainment.

B. Contours of mean streamwise velocity, Reynolds shear stress, and mean vorticity

Figure 3 compares the isocontours of mean streamwise velocity, Reynolds shear stress, and mean spanwise vorticity for the two extreme offset height ratios. The isocontours of the normalized mean streamwise velocity U/U_j for $h/d = 1$ and 4 are shown in Figs. 3(a) and 3(b), respectively. It should be noted that in Fig. 3(b) the vertical axis is terminated at $y/d = 2$ and not $y/d = 4$ in order to maintain the same interval of 5 as in Fig. 3(a). The plots indicate that the effect of confinement is to reduce the outward growth of the jet in the upper shear layer relative to the lower shear layer. This effect diminishes with increasing offset height ratio. The reduced growth of the jet at smaller depths suppresses mixing in the near-exit region, leading to larger extents of the potential core. The contours also provide an indication that after exiting the nozzle, the jet attaches to the free surface sooner at $h/d = 1$ than at $h/d = 4$. The values of distance L_R from the origin $x = 0$ to the attachment point are summarized in Table I for all four offset height ratios. When normalized by the nozzle width, a monotonic increase with h/d is observed. When normalized by the offset height, the L_R is of the same magnitude as the offset height for $h/d = 1$. At offset heights larger than 1, L_R is about three times as large as the offset height. Figures 3(c) and 3(d) show the isocontours of the normalized Reynolds shear stress $-\overline{u'v'}/U_j^2$ at $h/d = 1$ and 4, respectively. The plots show a negative distribution in the upper shear layer and a positive distribution in the lower shear layer, mimicking the direction of the mean streamwise velocity gradient in the shear layers. The plots indicate that the effect of the free surface is to reduce the spread of the Reynolds shear stress distribution in the upper shear layer compared to the lower shear layer. Isocontours of the normalized mean spanwise vorticity $\Omega_z d/U_j$ for the two cases are shown in Figs. 3(e) and 3(f). The mean spanwise vorticity reaches peak values in the near-exit region and has shear layer distributions that are of opposite sign to the Reynolds shear stress. At $h/d = 1$, the stronger confinement by the free surface stretches the upper shear layer contours almost parallel to the surface. With increasing offset height ratio, this effect is relaxed so that the contours recover their streamwise inclination to the axis. The contours show a damping effect on the mean spanwise vorticity in the upper shear layer due to the confinement in comparison to the lower shear layer. At larger offset height ratios, the mean spanwise vorticity is generally lower than corresponding values at smaller offset height ratios. For $h/d = 1$, the presence of finite vorticity near the free surface would be expected to have a significant impact on the energy redistribution mechanism at the free surface.

C. Jet maximum mean velocity decay and spreading characteristics

The streamwise evolution of the mean centerline velocity is shown in Fig. 4 for the four offset height ratios. Figure 4(a) shows the profiles of the maximum mean streamwise velocity normalized by the jet exit velocity U_j and the streamwise distance normalized by the nozzle width d. The solid lines in the plots correspond to a least-squares fit of the straight line

$$\frac{U_j}{U_m} = K_d\left(\frac{x}{d} - \frac{x_o}{d}\right) \tag{1}$$

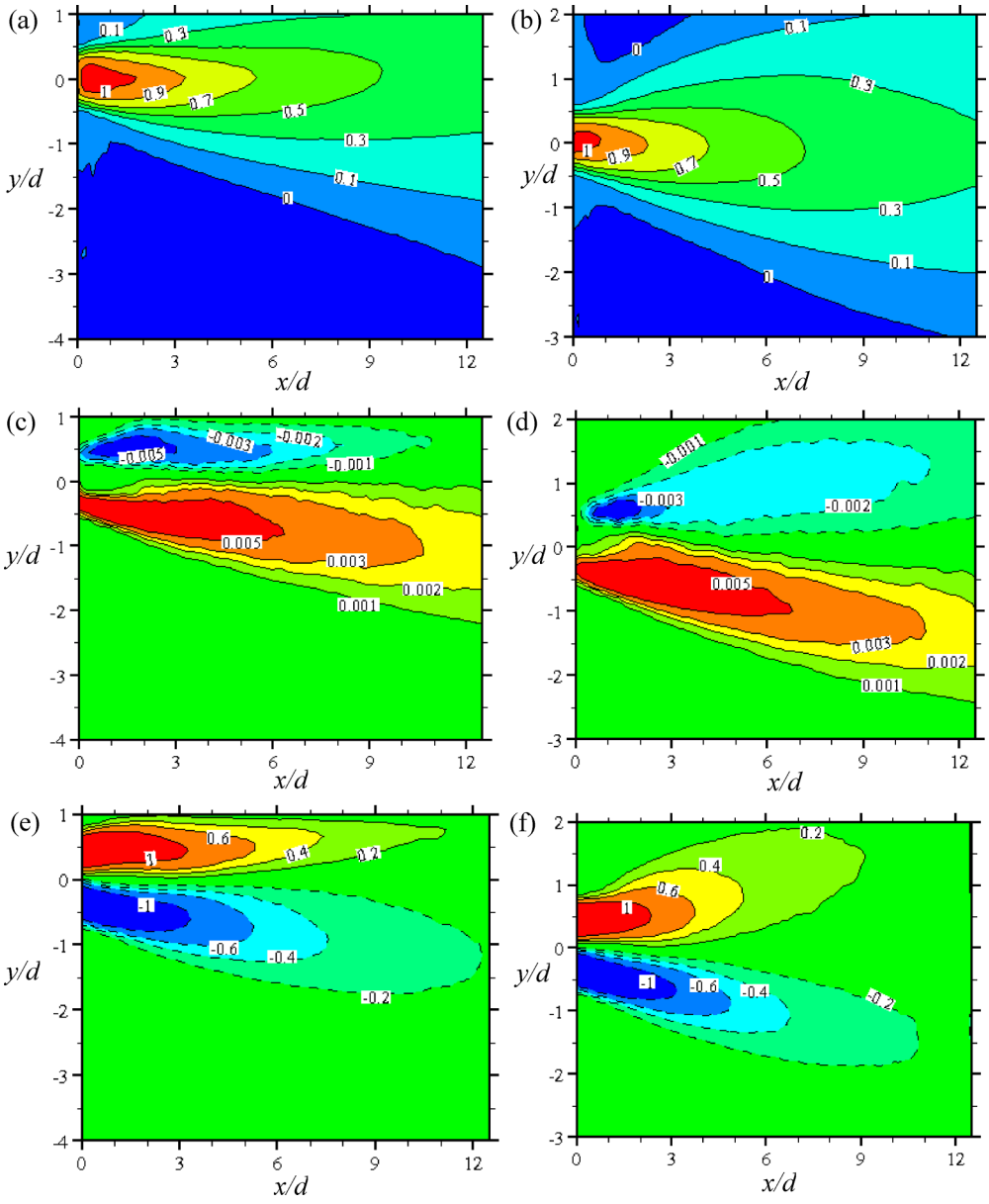

FIG. 3. Isocontour of mean streamwise velocity, U/U_j, Reynolds shear stress, $-\overline{u'v'}/U_j^2$ and mean spanwise vorticity, $\Omega_z d/U_j$ for the jet configurations $h/d = 1$ and $h/d = 4$. (a) Isocontours of U/U_j for $h/d = 1$; (b) Isocontours of U/U_j for $h/d = 4$; (c) Isocontours of $-\overline{u'v'}/U_j^2$ for $h/d = 1$; (d) Isocontours of $-\overline{u'v'}/U_j^2$ for $h/d = 4$; (e) Isocontours of $\Omega_z d/U_j$ for $h/d = 1$; (f) Isocontours of $\Omega_z d/U_j$ for $h/d = 4$.

to the measured data in the range $5 \leqslant x/d \leqslant 23$, where the slope K_d of the line represents the far-field mean streamwise velocity decay rate and the constant x_o represents kinematic virtual origin of the jet. The profiles indicate that the mean streamwise velocity decay scales with the classical variables U_j and d only for $h/d \geqslant 3$. With reduced offset height ratio, the jet entrainment rate diminishes, resulting in increasingly lower mean velocity decay rates compared to the deeper jets. The fitted values of the decay parameter K_d are summarized in Table II. The present values of K_d

TABLE I. Summary of values of the attachment length.

h/d	L_R/d	L_R/h
1	1.0	1.0
2	6.4	3.2
3	9.3	3.1
4	12.3	3.0

for $h/d \geqslant 3$ are about 4%–5% larger than the value of 0.203 reported by Mi and Nathan [28] for the free jet issuing from a sharp-edged square nozzle and are substantially ($\approx$27%−30%) larger than the round jet value of 0.167 for $h/d \approx 3.5$ [15]. The decay rate of $K_d = 0.176$ for $h/d = 2$ is similar to the value of 0.170 reported for a sharp-edged circular nozzle [19] submerged at the same offset height. Figure 4(b) shows the maximum mean streamwise velocity decay profiles with U_m and x normalized using the similarity variables proposed by Madnia and Bernal [15], $U_j d/h$ and h, respectively. Also included in the plots for reference are data from Sankar *et al.* [18] measured at $h/d = 1$ and 3. The similarity scaling performs a better job of collapsing the data for $h/d \geqslant 2$. At $h/d = 1$, the profiles undergo a change in slope at the location $x/h \approx 11$. This downstream location, representing the point of crossover from the jets at offset height ratio $h/d \geqslant 2$ to the jets at $h/d = 1$, corresponds to the location where the shear layer interacts with the free surface the most. The slope

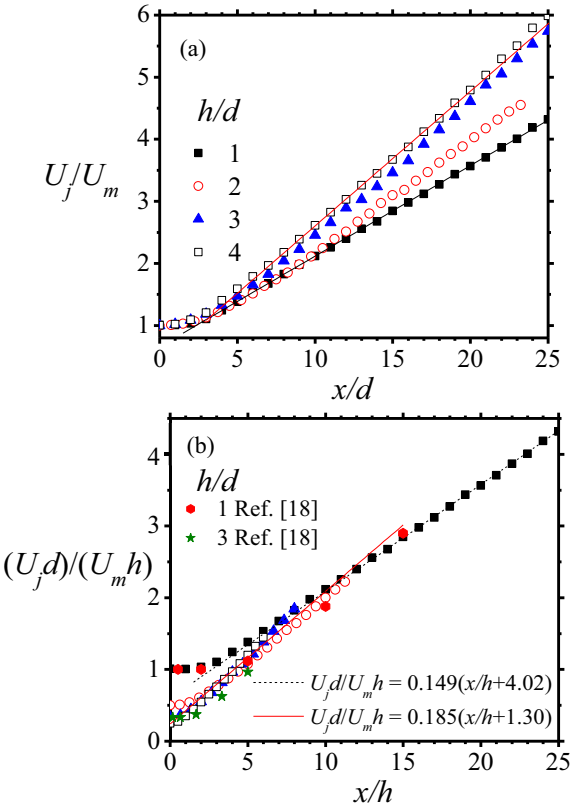

FIG. 4. Streamwise evolution of the maximum mean streamwise velocity decay U_j/U_m: (a) mean streamwise velocity decay in classical scaling and (b) mean streamwise velocity decay in similarity variables.

TABLE II. Summary of the jet mean streamwise velocity decay parameters.

h/d	K_d	Range
1	0.149	$5 \leqslant x/d \leqslant 23$
2	0.176	$5 \leqslant x/d \leqslant 23$
3	0.213	$5 \leqslant x/d \leqslant 23$
4	0.217	$5 \leqslant x/d \leqslant 23$

change at $h/d = 1$ indicates a stronger interaction between the shear layer and the free surface for these jets compared to the deeper jets. Based on the image jet model of Madnia and Bernal [15], the straight line

$$\frac{U_j d}{U_m h} = \frac{K_{d,f}}{\sqrt{2}}\left(\frac{x}{h} - \frac{x_o}{h}\right) \tag{2}$$

was fitted to the profiles in Fig. 4(b), where $K_{d,f}$ is the decay rate of the corresponding free jet, assumed herein to be approximately equal to 0.217, with a scaling factor of $\sqrt{2}$ introduced to account for the momentum of the image jet above the free surface. The least-squares fit of Eq. (2) to the data yields slopes of approximately 0.185 for $h/d \geqslant 2$ and 0.149 for $h/d = 1$. As noticed in previous investigations [15,17], for the shallow jet ($h/d = 1$), the slope 0.149 is in reasonable agreement with the value of $0.217/\sqrt{2}$ ($\approx$0.153).

Figure 5 examines the amount of deflection and streamwise growth of the jet. In Fig. 5(a) the extent of jet deflection is quantified in terms of the displacement of the location of the local

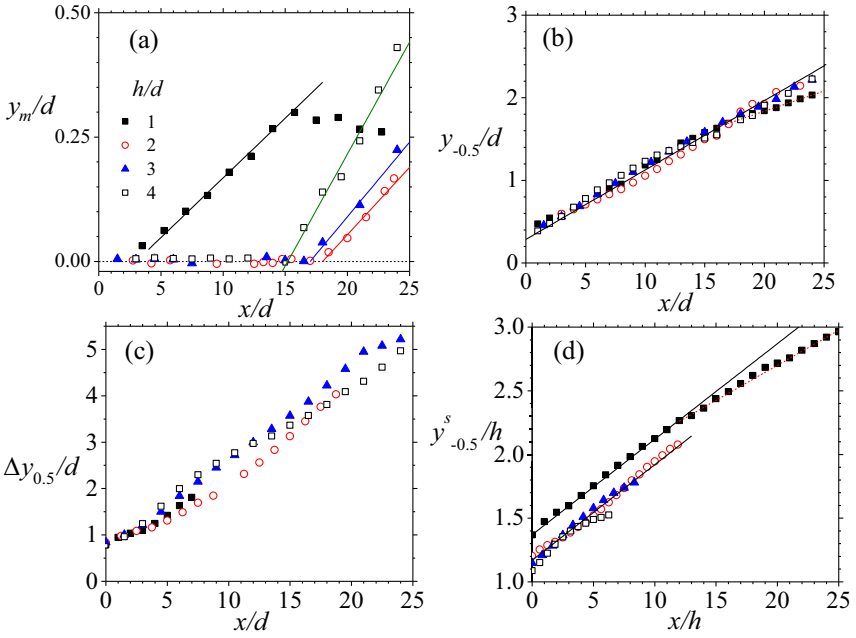

FIG. 5. (a) Location of the maximum mean streamwise velocity as a function of x/d. Solid lines denote least-squares linear fits to the y_m/d distributions. Also shown is the streamwise evolution of the normalized jet half-velocity widths: (b) profiles of the half-width distributions in the lower shear layer, (c) profiles of the jet width, and (d) profiles of jet half-width measured from the free surface to the half-velocity location in the lower shear layer. Lines in (b) and (d) denote the least-squares linear fits to the half-width distributions.

maximum mean streamwise velocity from the nozzle centerline (y_m). For $h/d \geqslant 2$, the location of the maximum mean streamwise velocity remains approximately on the nozzle centerline for a considerably longer streamwise distance ($x/d \approx 16 \pm 6\%$), after which the jet is deflected almost linearly towards the free surface. In the case of the shallow jet ($h/d = 1$), the close proximity to the free surface ensures that the jet deflection occurs shortly after exit from the nozzle. The amounts of deflection, represented by the slopes of the solid lines in Fig. 5(a), are 0.027, 0.030, and 0.045, for $h/d = 2$, 3 and 4, respectively. For $h/d = 1$, the jet has an intermediate region ($3 < x/d \leqslant 15$) in which the jet is deflected towards the free surface at a slope of approximately 0.024. Downstream of this region, y_m follows a nearly horizontal profile because the maximum mean streamwise velocity occurs relatively close to the free surface. The growth rate of the jet was quantified using the profiles of the half-velocity width. Figure 5(b) shows the streamwise evolution of the jet half-velocity width $y_{-0.5}$ measured from the location of U_m to the location below the jet axis where the mean streamwise velocity is half of the maximum mean streamwise velocity. The profiles indicate that the jet spreading rate in the lower shear layer is nearly independent of the offset height ratio for $h/d \geqslant 2$. A least-squares linear fit to the data within $5 \leqslant x/d \leqslant 23$ yields a slope or spreading rate of approximately 0.085. This value is not significantly different from free-jet values of 0.087 and 0.088 reported by Quinn and Militzer [29] and Obot *et al.* [30], respectively. For $h/d = 1$, the profile follows the others closely only within $x/d \leqslant 18$. Beyond $x/d \approx 18$, the jet is too close to the free surface to propagate and entrain ambient fluid. This leads to a reduced growth rate of about 0.049 due to the relatively strong confinement by the free surface in this case. The results presented in the literature [13,15] also show a similar change in slope at small offset height ratios in the interaction region. Figure 5(c) shows the streamwise evolution of the normalized width of the jet, estimated as the distance between the half-velocity locations in the upper and lower shear layers. The profiles increase linearly with streamwise distance but do not show any systematic dependence on the offset height ratio. Figure 5(d) shows the profiles of the jet half-width $y^s_{-0.5}$ measured from the free surface to the half-velocity location below the jet axis, as a function of x/h. Within the streamwise range $x/h < 13$, use of the similarity scaling h results in approximately linear distributions, with $y^s_{-0.5}/h$ values that are approximately 17% larger for $h/d = 1$ than for $h/d \geqslant 2$. Within this range least-squares line fits to the distributions give spreading rates of approximately 0.075. For $h/d = 1$, this value reduces to approximately 0.055 for $x/h > 11$. Madnia and Bernal [15] reported a slope of 0.078 for $x/h < 24$ using this scaling, followed by a slight decline for $x/h \geqslant 24$.

D. Turbulence intensities along the jet centerline

The variations of the streamwise and surface-normal turbulence intensities along the jet centerline are shown in Fig. 6. The corresponding centerline turbulence intensities from the smoothly contracting submerged square nozzle of Sankar *et al.* [18] are also included for comparison. The streamwise and surface-normal turbulence intensities normalized by the jet exit velocity are depicted in Figs. 6(a) and 6(b), respectively. A steep increase is observed in both turbulence intensities in the initial region ($x/d < 5$). This increase is considered to be an artifact of the large-scale coherent structures arising from the Kelvin-Helmholtz instability of the shear layer in the initial region [8] and the concomitant high turbulence production associated with large mean velocity gradients in this region. In the plots, the peak turbulence intensities occur at locations coinciding with the downstream end of the potential core regions. For the streamwise turbulence intensity, although no significant change occurs in the peak value from $h/d = 1$ to $h/d = 2$, moderate enhancements of 24% and 40% are observed for $h/d = 3$ and 4, respectively. The increase in the peak value of the surface-normal turbulence intensity is smaller (about 9%–12%). For a given offset height ratio, the Sankar *et al.* [18] results peak at substantially higher values, albeit at a more gradual rate than the present data. The more gradual rise and higher peak values of the reference results can be attributed to the differing upstream conditions in that case, that is, smoothly contracting nozzle and higher Reynolds number (40 000). After the initial region, the intensities then decrease to final values that are nearly independent of offset height ratio. From Figs. 6(a) and 6(b) it is evident that during the

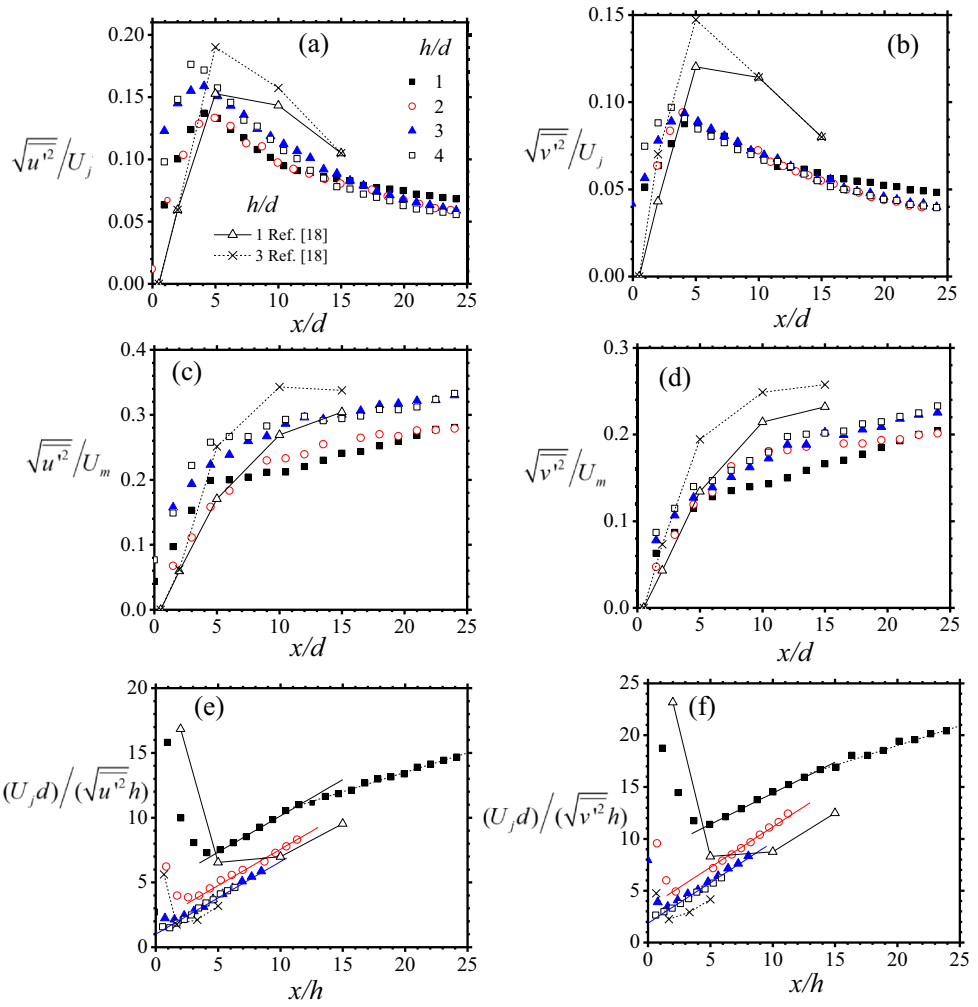

FIG. 6. Streamwise evolution of the streamwise and surface-normal turbulence intensities along the jet centerline: (a) streamwise and (b) surface-normal turbulence intensities normalized with the jet exit velocity and streamwise distance normalized with the nozzle width, (c) streamwise and (d) surface-normal turbulence intensities normalized with the maximum mean velocity and streamwise distance normalized with the nozzle width, and (e) streamwise and (f) surface-normal turbulence intensities normalized with the similarity variables.

jet development the magnitude of $\sqrt{\overline{v'^2}}/U_j$ is always less than that of $\sqrt{\overline{u'^2}}/U_j$, which provides an indication of anisotropy of the Reynolds stress or turbulence intensity components in the jets. When normalized by the local maximum mean streamwise velocity [Figs. 6(c) and 6(d)], increasingly higher values are observed in the far-field region, due to the decreasing local mean streamwise velocities. In the far field of the jet, no discernible differences are observed between $h/d = 1$ and 2 and between $h/d = 3$ and 4, but as indicated by the results of Sankar *et al.* [18], the far-field turbulence intensities of the deeper jets ($h/d = 3$ and 4) are about 18%–20% larger than those of the shallower jets ($h/d = 1$ and 2). At $x/d = 23$, the streamwise and surface-normal turbulence intensities for $h/d \geqslant 3$ are approximately 33% and 23%, respectively. The corresponding far-field streamwise and transverse turbulence intensity values reported for square free jets are, respectively, 22% and 20% [8,29]. The disparity between the present two values can be attributed to the strong anisotropy of Reynolds stresses in the free-surface jets.

Figures 6(e) and 6(f) show the profiles of the centerline streamwise and surface-normal turbulence intensities normalized by the similarity variables $U_j d/h$ and h. Because of the initial rise and fall of the centerline $\sqrt{\overline{u'^2}}/U_j$ and $\sqrt{\overline{v'^2}}/U_j$ values [see Figs. 6(a) and 6(b)], minima occur in the profiles. Also, because of the tendency of the similarity scaling to reduce scatter in the data, the locations of the minimum values are more clearly defined. These locations, corresponding to the potential core lengths, are evidently at increasingly larger streamwise distances with decreasing offset height ratio, as suggested by the streamwise mean velocity contours [Figs. 3(a) and 3(b)]. The profiles in Figs. 6(e) and 6(f) show a change in slope around the location of the minimum value, collapse at larger offset height ratios ($h/d = 3$ and 4), and enhancements with further reduction in offset height ratio. Downstream of the minimum value, the slope of the streamwise turbulence intensity profiles, estimated from a least-squares linear fit to the data, is approximately 0.560. This is about 25% lower than the value of 0.739 measured by Madnia and Bernal [15] for their submerged round jet. For the shallow jet ($h/d = 1$), a further change in slope to a value of approximately 0.300 can be observed at $x/h \approx 11$. In the case of the surface-normal turbulence intensity, the slopes are slightly larger: 0.780 for $h/d \geqslant 2$ and 0.600 for $h/d = 1$, which reduces to 0.380 beyond $x/h \approx 11$. At $h/d = 1$, the observed changes in slope of the turbulence intensity profiles at $x/h \approx 11$ is consistent with the changes in slope of the corresponding mean streamwise velocity decay profile in Fig. 4(b) and the half-width distribution in Fig. 5(d).

E. Surface mean velocity and turbulence intensities

Figure 7 shows profiles of the mean streamwise surface velocity U_s and surface velocity defect $\Delta U = U_m - U_s$. It should be pointed out that although the free surface was captured by the PIV imaging, its exact location was not known *a priori*. The position of the free surface was recovered from the processed images by examining several groups of mean streamwise velocity profiles plotted along horizontal lines near the upper edge of the FOV. By restricting the search to the region extending ten vector spacings from the upper edge of the FOV, if at a given elevation no significant variations occur in relation to the profiles above and below the elevation to within measurement uncertainty, that location was taken as the position of the free surface. For all the plots in Fig. 7, the streamwise distance is first shifted by the attachment length so that the origin is now at the attachment point x_r. The shifted distance is then normalized by the jet offset height. Profiles of the mean streamwise surface velocity normalized by the jet exit velocity are presented in Fig. 7(a) for the four offset height ratios. Upstream of the attachment point, the mean streamwise velocity values are negligibly small. Downstream of the attachment point (interaction region), the mean surface velocity is nonzero. Within the region $(x - x_r)/h < 10$, the mean surface flow accelerates to its maximum velocity by amounts that increase with decreasing offset height ratio. Further downstream, the jet is decelerating for $h/d = 1$, 2, and 3. For $h/d = 4$, because this is the case with the least shear layer–free-surface interaction, the flow is accelerating almost linearly. In the absence of mean surface deformation, the surface flow can be described as being in a state of strain due to the alternating acceleration ($\partial U_s/\partial x > 0$) and deceleration ($\partial U_s/\partial x < 0$) and the effect is more dramatic as the offset height is reduced. Figure 7(b) shows profiles of the mean surface velocity defect, normalized by the local maximum mean streamwise velocity U_m. The profiles show a good collapse for the chosen velocity scale and follow the exponential-Gaussian distribution

$$y^* = 0.02 + \exp\left(\frac{-x^{*2}}{3.92 + 5.8x^*}\right), \tag{3}$$

where $y^* = \Delta U/U_m$ and $x^* = (x - x_r)/h$. Figure 7(c) shows the profiles of the mean streamwise surface velocity normalized by the similarity scaling of Madnia and Bernal [15]. The similarity scaling collapses the profiles only over a limited extent of the interaction region [$(x - x_r)/h < 5$]. When the mean surface velocity defect is normalized by the similarity scaling [Fig. 7(d)], the profiles collapse in the interaction region.

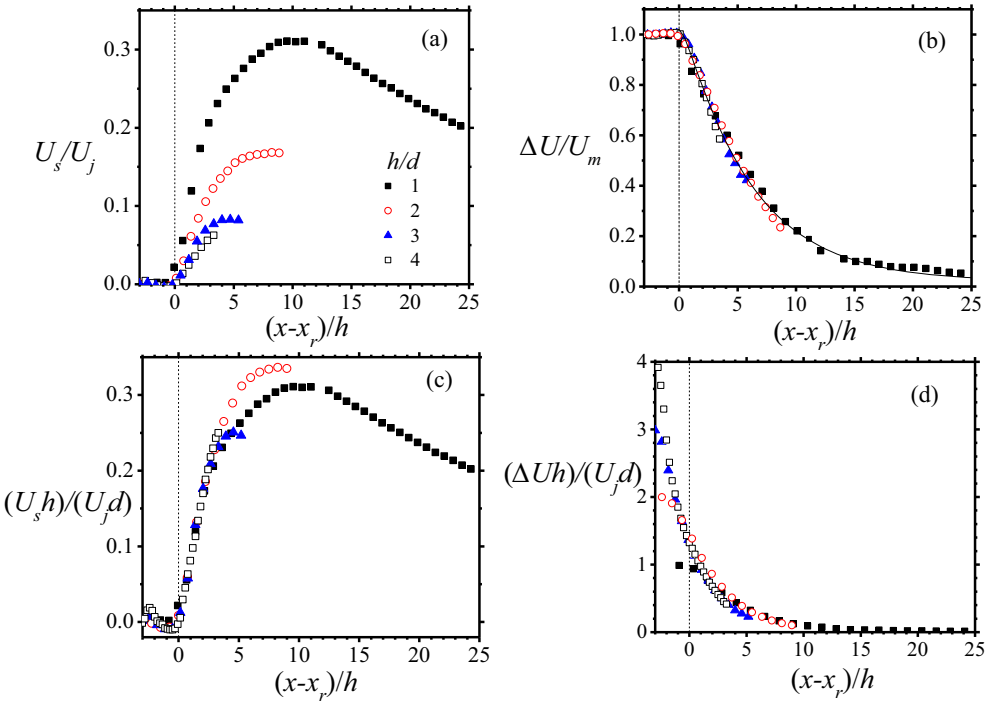

FIG. 7. Streamwise evolution of the mean streamwise surface velocity and mean streamwise surface velocity defect: (a) mean streamwise surface velocity normalized by the jet exit velocity, (b) mean surface velocity defect normalized by the maximum mean streamwise velocity, (c) mean streamwise surface velocity normalized by similarity variables, and (d) mean surface velocity defect normalized by similarity variables. The distance $x-x_r$ represents the streamwise distance shifted relative to the attachment point. The solid line in (b) is the least-squares fit of the exponential-Gaussian hybrid distribution.

The streamwise and surface-normal turbulence intensity profiles at the free surface are shown in Fig. 8. Figure 8(a) shows the streamwise surface turbulence intensity normalized by the jet exit velocity. The profiles indicate that effect of decreasing the offset height ratio is to augment the streamwise surface turbulence intensity levels. Except for $h/d = 1$, all profiles develop single peaks near the attachment point. For the $h/d = 1$ jet, two peaks are observed, one near the attachment point and a much broader one near the middle of the interaction region. This second peak is related to the stronger interaction between the $h/d = 1$ jet and the free surface, as foreshadowed by the changes in slope of the mean velocity and turbulence intensity profiles at $x/h \approx 11$. The corresponding profiles of the surface-normal turbulence intensity show a similar enhancement with decreasing offset height ratio [Fig. 8(b)], except for a rapid decay with downstream distance as the jet propagates through the interaction region. This damping effect of the free surface on the surface-normal component is an indication of the turbulent kinetic energy (TKE) redistribution at the free surface from the surface-normal component to streamwise component [16,17]. As indicated by the plots, this TKE redistribution mechanism would be enhanced with decreasing offset height ratio. The turbulence intensities normalized by the maximum mean streamwise velocity U_m are plotted in Figs. 8(c) and 8(d) to check for plausible scaling with U_m. It is apparent that the maximum mean streamwise velocity is not the appropriate velocity scale for the surface turbulence intensities. Figure 8(e) shows the profiles of the streamwise surface turbulence intensity normalized by the mean surface velocity defect. The profiles collapse reasonably well onto a single curve represented by the exponential

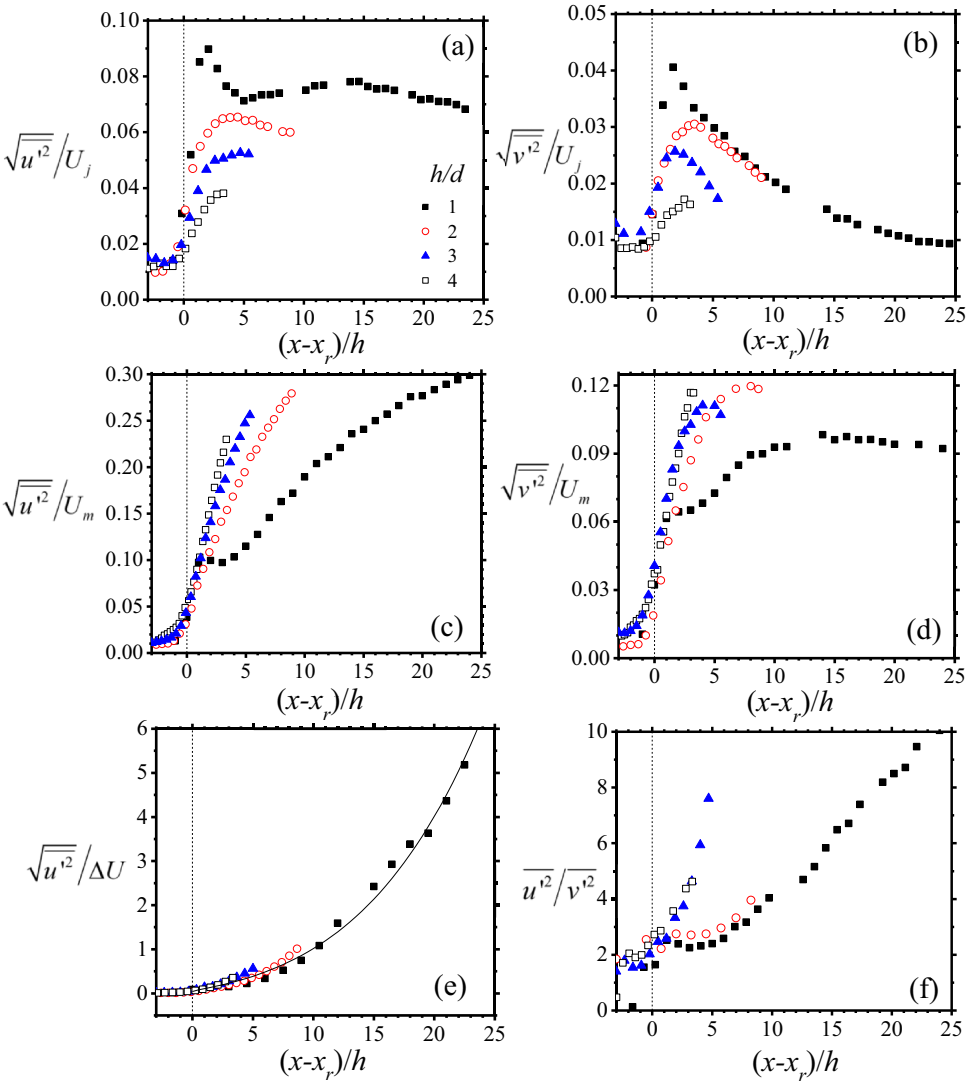

FIG. 8. Streamwise evolution of the streamwise and surface-normal turbulence intensities at the free surface: (a) and (b) surface turbulence intensities normalized by the jet exit velocity, (c) and (d) surface turbulence intensities normalized by the maximum mean streamwise velocity, (e) surface streamwise turbulence intensity normalized by the mean surface velocity defect, and (f) stress ratio at the free surface. The horizontal distance is shifted as in Fig. 7. The solid line in (e) is a least-squares fit of the exponential distribution $y^{**} = 0.04\exp(x^{*0.51})$.

distribution (solid line)

$$y^{**} = 0.04\exp(x^{*0.51}), \tag{4}$$

where y^{**} denotes the dimensionless streamwise turbulence intensity at the free surface. The substantially lower values of the surface-normal component [Figs. 8(b) and 8(d)] compared to the streamwise component [Figs. 8(a) and 8(c)] indicate strong anisotropy in the Reynolds stress field at the free surface. Figure 8(f) shows profiles of the stress ratio at the free surface. For the deeper jets, the stress ratio increases monotonically in the interaction region. In the case of the shallow jets, an initial decrease occurs during the initial interaction, followed by a monotonic increase downstream

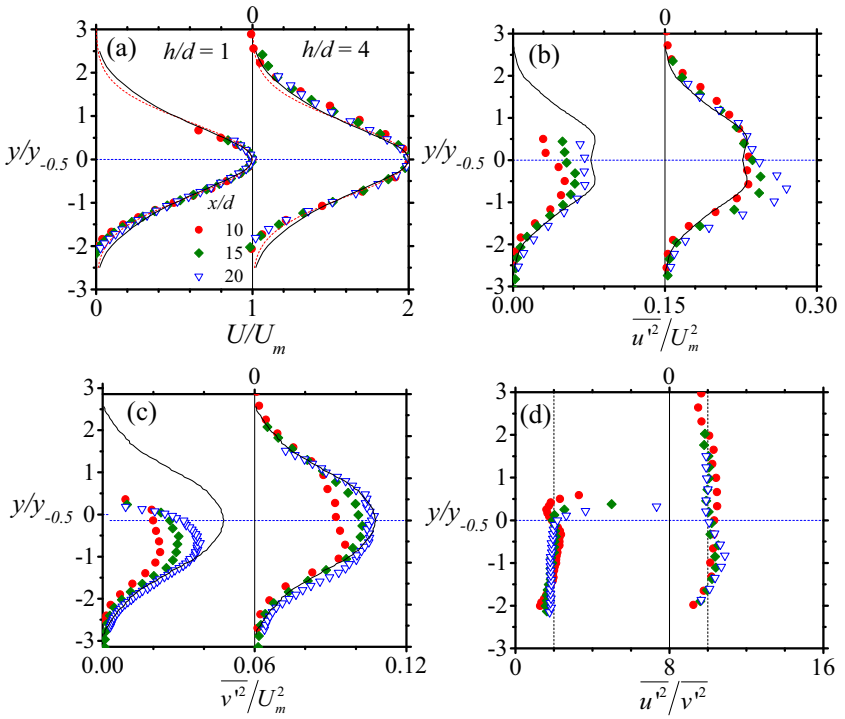

FIG. 9. Similarity scaling of the mean velocity and normal Reynolds stresses: (a) mean streamwise velocity profiles, (b) streamwise Reynolds stress profiles, (c) surface-normal Reynolds stress profiles, and (d) stress ratio profiles. Solid lines denote similarity profiles from the round jet data of Hussein *et al.* [5]; dashed lines in (a) denote the Gaussian mean streamwise velocity distribution.

of the initial interaction. The initial decrease of the stress ratio for the shallow jets can be attributed to the more dramatic increase in the surface-normal velocity fluctuations than the streamwise velocity fluctuations during the initial interaction.

F. Similarity profiles of the mean velocity and Reynolds stresses

Figure 9 shows a comparison of the one-dimensional profiles of the mean velocity and Reynolds stresses at various streamwise locations in the interaction region. In all cases, the surface-normal distance is normalized by the local half-width value $y_{-0.5}$, while the mean velocity and Reynolds stresses are normalized by U_m and U_m^2, respectively. Figure 9(a) shows profiles of the mean streamwise velocity at the three successive streamwise locations $x/d = 10, 15$, and 20 for $h/d = 1$ and 4. The dashed and solid lines correspond to the Gaussian distribution and the similarity profile from a round free-jet hot-wire experiment [5], respectively, included for comparison. The mean velocity profiles exhibit self-similarity in the interaction region. The profiles also compare well with the Gaussian and Hussein *et al.* [5] distributions for both offset height ratios, except near the edge of the lower shear layer where the present values are about 5%–10% lower. These discrepancies can be attributed to the presence of recirculation near the lower wall of the test section. For the streamwise and surface-normal Reynolds stresses shown in Figs. 9(b) and 9(c), respectively, the peak values are increasing with streamwise distance, in agreement with the literature on turbulent free jets [2]. The literature shows that the second-order moments do not attain self-similarity until some 50–70 diameters downstream of the nozzle. For a given streamwise location, the effect of decreasing offset height ratio is to decrease the peak values of the Reynolds stresses. Figure 9(d) shows the similarity profiles of the stress ratio. For isotropic turbulence, this ratio is approximately 1. The present values

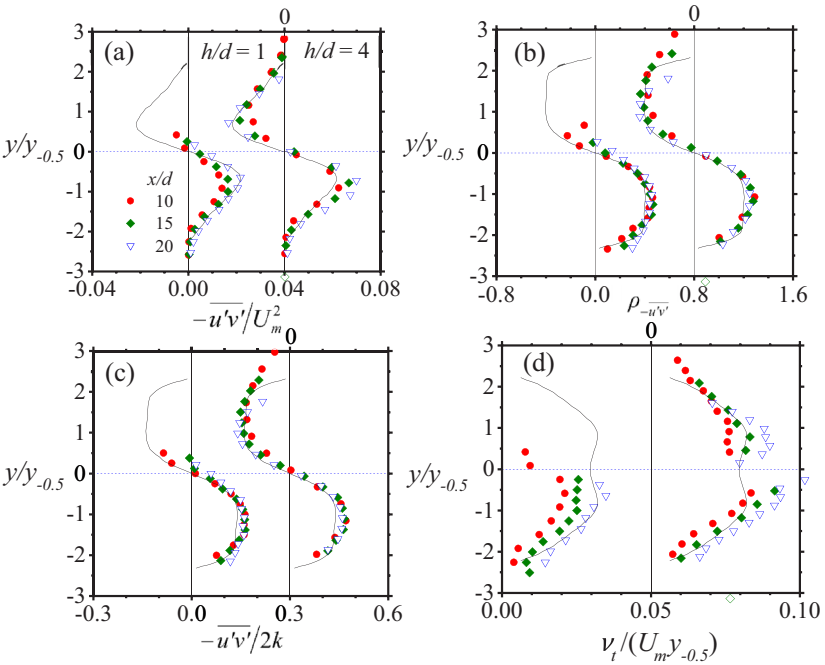

FIG. 10. Similarity scaling of the Reynolds shear stress and stress ratios: (a) Reynolds shear stress profiles, (b) Reynolds shear stress correlation coefficient, (c) structure parameter, and (d) eddy viscosity. Solid lines are as in Fig. 9.

of the stress ratio are within $2.0 \pm 10\%$ over most of the flow region, except in the immediate vicinity of the free surface. Near the free surface, the stress ratio is increasing with streamwise distance due to the damping effect of the surface on the surface-normal component in the interaction region.

Figure 10 shows the similarity profiles of the normalized Reynolds shear stress and related quantities in the interaction region. The Reynolds shear stress profiles at the three streamwise locations are shown in Fig. 10(a). For $h/d = 4$, the profiles exhibit the same antisymmetric shape as the free-jet distribution. Although the peak values are increasing with streamwise distance, the effect is less dramatic than was observed for the normal stresses. Also, because of the enhanced mixing in the lower shear layer the peak values are about 50%, 53%, and 25% larger than corresponding peak values in the upper shear layer. At $h/d = 1$, the increased confinement further reduces the peak Reynolds shear stress to either substantially lower values or nearly zero in the upper shear layer. The negligible values of the Reynolds shear stress in the upper shear layer of the shallow jet can be attributed to damping of the mean shear by the increased confinement. Profiles of the Reynolds shear stress correlation coefficient $\rho_{-\overline{u'v'}} = -\overline{u'v'}/(\overline{u'^2 v'^2})^{0.5}$ are shown in Fig. 10(b). At both offset height ratios, the profiles show good agreement with the free-jet values in the lower shear layer, with peak values of approximately $0.41 \pm 5\%$. In the upper shear layer a similar peak value occurs for $h/d = 4$, but the profiles deviate significantly from that of the free jet near the free surface. At the lower offset height ratio, the damping effect on the Reynolds shear stress produces a commensurate diminishing effect on the correlation coefficient. Figure 10(c) shows profiles of the structure parameter $a_1 = -\overline{u'v'}/2k$, where k is the turbulent kinetic energy. Values of the turbulent kinetic energy were estimated as $k = 0.5(\overline{u'^2} + 2\overline{v'^2})$. The profiles exhibit the same qualitative trend as the correlation coefficient, but with peak values of approximately 0.15. This value of a_1 corresponds to a k-ε Reynolds-averaged Navier-Stokes modeling coefficient $C_\mu[\approx(-\overline{u'v'}/k)^2]$ of approximately 0.09. For $h/d = 1$, this coefficient is nearly zero in the upper shear layer, implying

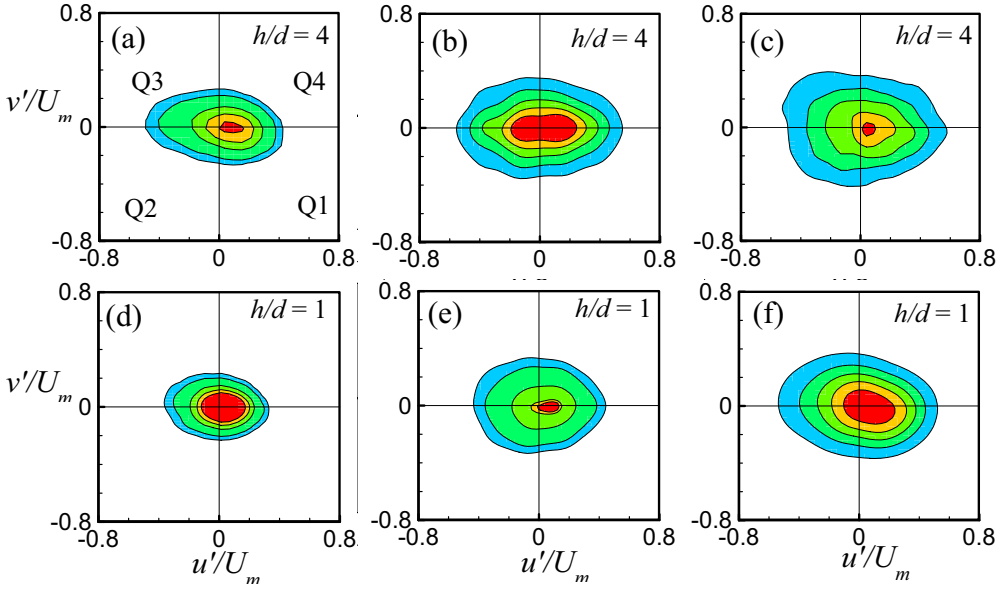

FIG. 11. Streamwise evolution of the joint probability density functions at the jet centerline: (a) joint PDF contours at $x/d = 3$ for $h/d = 4$, (b) joint PDF contours at $x/d = 9$ for $h/d = 4$, (c) joint PDF contours at $x/d = 20$ for $h/d = 4$, (d) joint PDF contours at $x/d = 3$ for $h/d = 1$, (e) joint PDF contours at $x/d = 9$ for $h/d = 1$, and (f) joint PDF contours at $x/d = 20$ for $h/d = 1$. Contour levels are from 0.5 to 2.5 at intervals of 0.5.

that $C_\mu = 0.09$ may not be suitable for surface-attaching jets of low offset height ratios. Figure 10(d) shows profiles of the eddy viscosity $v_t/(U_m y_{-0.5})$. The plots indicate that the eddy viscosity is an increasing function of downstream distance in the interaction region and decreases with decreasing offset height ratio.

G. Confinement effects on the turbulence structure

1. Joint probability density functions

The joint probability density function (PDF) $p(u',v')$ defined as (Wallace and Brodkey [31])

$$\overline{u'v'} = \int \int_{-\infty}^{\infty} u'v' P(u',v') du' dv' \tag{5}$$

is often used to investigate the correlation between the instantaneous velocity fluctuations. The joint PDFs were estimated by sorting the velocity fluctuations into equal-width 100×100 bins. Figure 11 shows the streamwise evolution of the joint PDF of u' and v' for $h/d = 1$ and 4. The isocontours were plotted at the three streamwise locations $x/d = 3, 9$, and 20. The surface-normal location in each case corresponds to the location of the local maximum mean streamwise velocity (y_m). As shown in Fig. 11(a), the straight lines passing through the origin divide the plots into the four quadrants of the u'-v' plane: Q1, Q2, Q3, and Q4, where Q1 $(u',-v')$ denotes fast entrainment of ambient fluid, Q2 $(-u',-v')$ denotes slow entrainment of ambient fluid, and Q3 $(-u',v')$ and Q4 (u',v') denote slow and fast ejections, respectively. At this surface-normal location, the contours are almost elliptical and show no preferred orientation for any of the four quadrants. A streamwise growth of the probability contours is observed in both cases, suggesting the increasing importance of extreme Reynolds shear stress producing events. The slight shift of the maximum probability in favor of the u' direction indicates a dominance of fast u' fluctuations in generating the Reynolds shear stress at y_m. For a given streamwise location, the effect of reducing the offset height ratio is to diminish

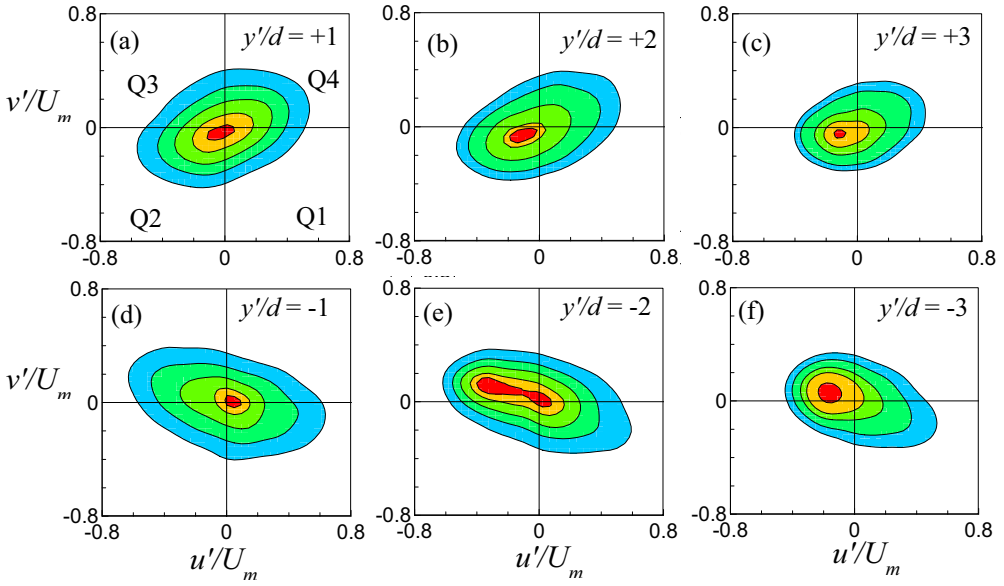

FIG. 12. Variation of the joint probability density functions within upper and lower shear layers of the $h/d = 4$ jet at $x/d = 20$: (a) joint PDF contours at $y'/d = 1$, (b) joint PDF contours at $y'/d = 2$, (c) joint PDF contours at $y'/d = 3$, (d) joint PDF contours at $y'/d = -1$, (e) joint PDF contours at $y'/d = -2$, and (f) joint PDF contours at $y'/d = -3$. Contour levels are from 0.5 to 2.5 at intervals of 0.5.

the probability of extreme Reynolds shear stress producing events. This damping effect on the joint PDFs is consistent with the reduced Reynolds shear stress at smaller offset height ratios of the jet.

Figure 12 shows the joint probability density functions at $x/d = 20$ for $h/d = 4$ at various surface-normal locations: $y'/d = \pm 1, \pm 2, \pm 3$, where y' is the surface-normal distance measured relative to y_m. Thus, the plus sign denotes the distance measured towards the free surface, while the minus sign denotes the distance measured away from the free surface. Above the maximum mean velocity line [Figs. 12(a)–12(c)], the joint PDF contours are inclined towards quadrants Q2 and Q4, indicating slow entrainments and fast ejections to be the dominant contributors to the mean Reynolds shear stress ($-\overline{u'v'}$) in the upper shear layer. There is a diminishing effect in the direction of the free surface due to the decay in Reynolds shear stress as the free surface is approached. Also, as the free surface is approached, the maximum joint probability shifts in favor of Q2. Since the Reynolds shear stress must be approaching zero, a shift of the maximum in favor of one quadrant should be balanced by a corresponding increase in magnitude of the fluctuations in the opposite quadrant. This effect is depicted by the increasing contraction of the contour levels in Q2 and expansion of the contour levels in Q4. Figures 12(d)–12(f) show the corresponding joint PDF contours below the mean shear line (lower shear layer). The contour inclinations in this case are reversed as the contribution to the mean Reynolds shear stress shifts in favor of quadrants Q1 and Q3. The contours also indicate a diminishing effect in the direction away from the mean shear line, but they are wider in comparison with those in the upper shear layer. The larger contours in the lower shear layer are consistent with the larger Reynolds shear stress magnitudes in the lower shear layer.

To examine the relative contributions of the velocity fluctuations to the Reynolds shear stress, the values of the weighted joint probability density function (covariance integrand) $-u'v'P(u',v')$ were calculated. Figure 13 shows the isocontours of the weighted joint probability density function at three streamwise locations along the mean shear line ($y'/d = 0$). There is no systematic trend in the positive and negative distributions, except for the smaller lobes on the positive u' side, which are compensated for by the larger lobes on negative u' side of the horizontal axis. This mimics the joint PDF distributions shown in Fig. 11. It should be noted though that for $h/d = 1$, the contours

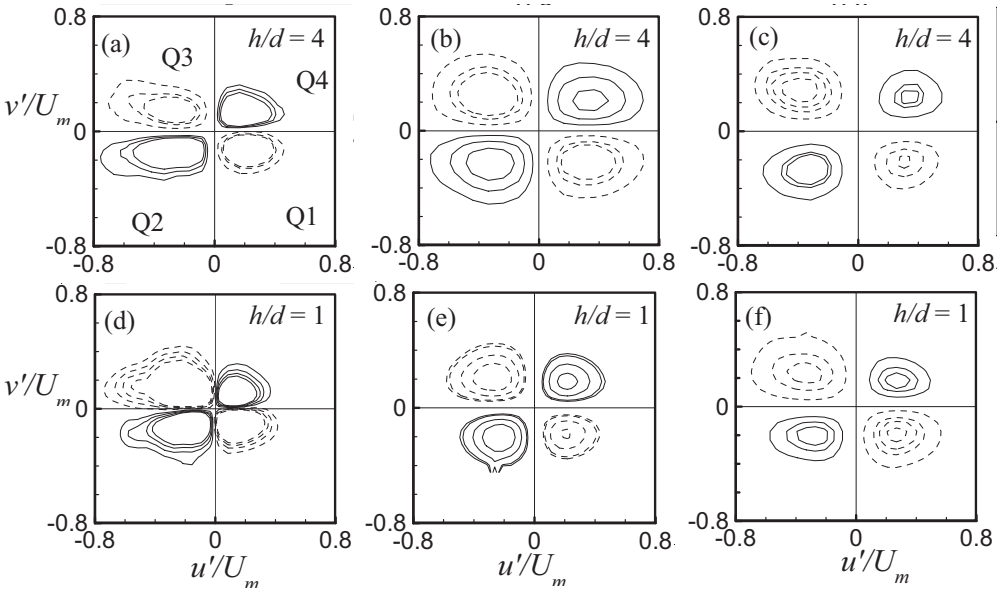

FIG. 13. Streamwise evolution of the weighted joint probability density functions at the jet centerline: (a) weighted joint PDF contours at $x/d = 3$ for $h/d = 4$, (b) weighted joint PDF contours at $x/d = 9$ for $h/d = 4$, (c) weighted joint PDF contours at $x/d = 20$ for $h/d = 4$, (d) weighted joint PDF contours at $x/d = 3$ for $h/d = 1$, (e) weighted joint PDF contours at $x/d = 9$ for $h/d = 1$, and (f) weighted joint PDF contours at $x/d = 20$ for $h/d = 1$. Contour levels vary from -0.0016 to 0.0016 at intervals of 0.0004.

at $x/d = 20$ indicate a slight orientation in favor of Q1 and Q3 [not quite obvious from Fig. 11(f)] that may be explained by the deflection of the jet away from the free surface at this location [see Fig. 5(a)].

The weighted joint probability density functions computed on either side of the maximum velocity line at $x/d = 20$ are shown in Fig. 14 for $h/d = 4$. In the upper shear layer, the positive PDFs are substantially larger than the negative PDFs, in agreement with the dominance of Q2 and Q4 events in this region. Towards the free surface, the weighted joint PDFs are diminishing as observed in the joint PDFs. In the lower shear layer, the negative PDFs are substantially larger than the positive PDFs and the same damping effect is observed away from the maximum mean velocity line.

2. Two-point correlations between the velocity fluctuations

The two-point correlations between the velocity fluctuations were estimated using the relation

$$R_{AB}(x_{\mathrm{ref}} + \Delta x, y_{\mathrm{ref}} + \Delta y) = \frac{\overline{A(x_{\mathrm{ref}}, y_{\mathrm{ref}})B(x_{\mathrm{ref}} + \Delta x, y_{\mathrm{ref}} + \Delta y)}}{\sigma_A(x_{\mathrm{ref}}, y_{\mathrm{ref}})\sigma_B(x_{\mathrm{ref}} + \Delta x, y_{\mathrm{ref}} + \Delta y)}, \tag{6}$$

where $A(x, y)$ and $B(x, y)$ are the two variables whose two-point correlation is required, $(x_{\mathrm{ref}}, y_{\mathrm{ref}})$ is the reference location, Δx and Δy are the spatial separations between A and B in the streamwise and surface-normal directions, respectively, and σ_A and σ_B are the root-mean-square values of A and B at $(x_{\mathrm{ref}}, y_{\mathrm{ref}})$ and $(x_{\mathrm{ref}} + \Delta x, y_{\mathrm{ref}} + \Delta y)$, respectively. Figure 15 shows the isocontours of the two-point autocorrelation function of the streamwise velocity fluctuation R_{uu} centered at $x/d = 3, 9$, and 20 for $h/d = 1$ and 4. The surface-normal location where the correlations were calculated corresponds to $y'/d = 0$. The plots indicate a monotonic increase in the spatial extents of R_{uu} that is consistent with the growth of the jet in the streamwise direction. For $h/d = 4$, the correlation contours are almost parallel to the free surface. For $h/d = 1$, the correlations, which are smaller for the most part, are parallel to the free surface, except at $x/d = 20$. At the location $x/d = 20$, the R_{uu} correlation

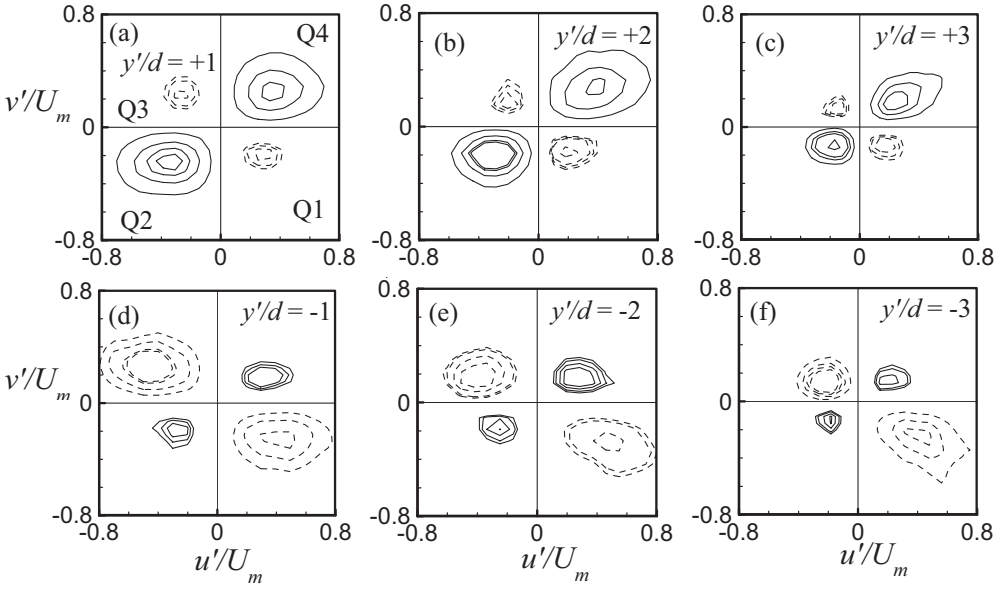

FIG. 14. Variation of the joint probability density functions within upper and lower shear layers of the $h/d = 4$ jet at $x/d = 20$: (a) weighted joint PDF contours at $y'/d = 1$, (b) weighted joint PDF contours at $y'/d = 2$, (c) weighted joint PDF contours at $y'/d = 3$, (d) weighted joint PDF contours at $y'/d = -1$, (e) weighted joint PDF contours at $y'/d = -2$, and (f) weighted joint PDF contours at $y'/d = -3$. Contour levels vary from -0.0016 to 0.0016 at intervals of 0.0004.

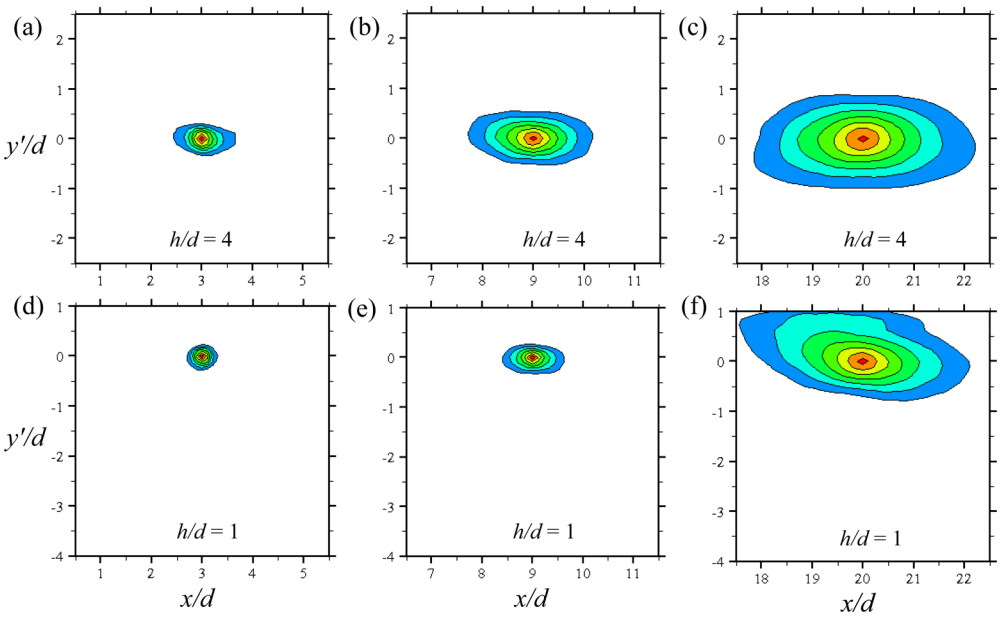

FIG. 15. Streamwise evolution of the streamwise velocity fluctuation autocorrelation function R_{uu} at the jet centerline: (a) R_{uu} contours at $x/d = 3$ for $h/d = 4$, (b) R_{uu} contours at $x/d = 9$ for $h/d = 4$, (c) R_{uu} contours at $x/d = 20$ for $h/d = 4$, (d) R_{uu} contours at $x/d = 3$ for $h/d = 1$, (e) R_{uu} contours at $x/d = 9$ for $h/d = 1$, and (f) R_{uu} contours at $x/d = 20$ for $h/d = 1$. Contour levels are from 0.3 to 0.9 at intervals of 0.1.

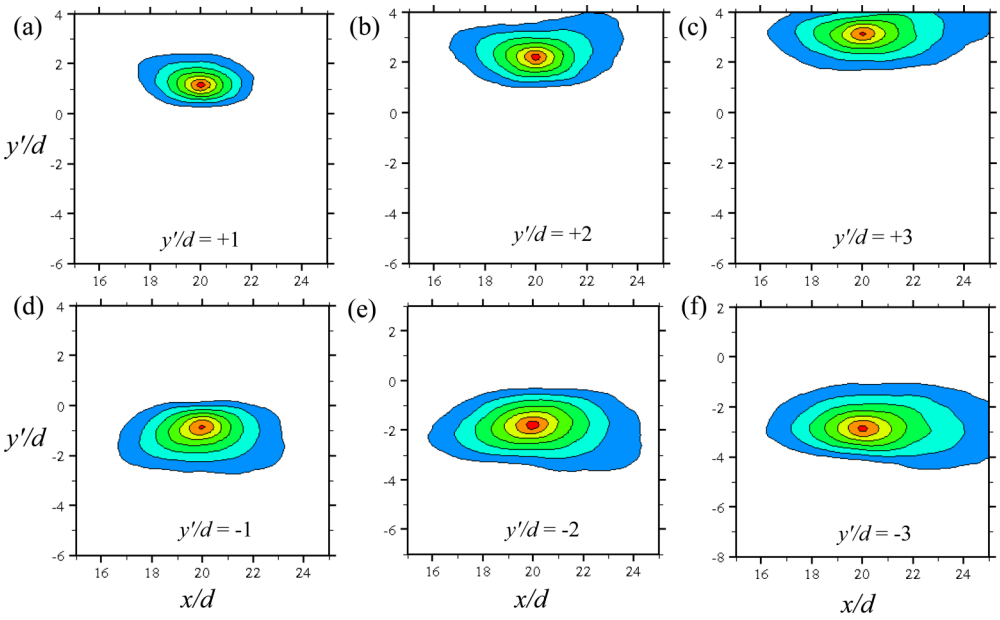

FIG. 16. Variation of the streamwise velocity fluctuation autocorrelation function R_{uu} within upper and lower shear layers for the $h/d = 4$ jet at $x/d = 20$: (a) R_{uu} contours at $y'/d = 1$, (b) R_{uu} contours at $y'/d = 2$, (c) R_{uu} contours at $y'/d = 3$, (d) R_{uu} contours at $y'/d = -1$, (e) R_{uu} contours at $y'/d = -2$, and (f) R_{uu} contours at $y'/d = -3$; Contour levels are from 0.3 to 0.9 at intervals of 0.1.

in this case is attached to the free surface and is inclined at angle of approximately 11.4°. This streamwise inclination is similar to the value of approximately 11° observed in wall jets [32] and zero-pressure gradient turbulent boundary layers [33].

Figure 16 shows the isocontours of R_{uu} at $x/d = 20$ for $h/d = 4$. In both halves of the shear layer the correlations are enhanced in the direction away from maximum velocity line. Nevertheless, in the upper shear layer, the surface confinement suppresses the correlation levels in comparison to those in the lower shear layer.

Figure 17 shows the isocontours of the two-point autocorrelation function of the surface-normal velocity fluctuation R_{vv} at $y'/d = 0$ for $h/d = 1$ and 4. These plots indicate a similar growth in the streamwise direction. However, there is a consistent reduction in the levels of R_{vv} for $h/d = 1$ compared to $h/d = 4$ irrespective of the downstream location, suggesting a stronger impact of the free surface for $h/d = 1$.

Figure 18 shows the isocontours of the R_{vv} correlation at $x/d = 20$ above and below the maximum velocity line for $h/d = 4$. In the upper shear layer [Figs. 18(a)–18(c)], the free surface suppresses the surface-normal two-point correlation function, as opposed to the enhancement observed in the streamwise counterpart in this region. This is consistent with the damping effect of the free surface on the surface-normal velocity fluctuations. In the lower shear layer [Figs. 18(d)–18(f)], the R_{vv} correlation is enhanced with distance away from maximum mean velocity line as was observed for R_{uu} in this region.

The influence of the jet confinement on the average size of the turbulent scales is examined in Fig. 19. The average size of the turbulent scales is quantified in terms of the streamwise and surface-normal extents of the two-point correlation contours. Figure 19(a) shows the functional dependence of the streamwise extent Lx_{uu} of R_{uu} on x/d. The streamwise extent of R_{uu} is defined herein as the distance between the self-correlation peak and the most downstream location on the $R_{uu} = 0.3$ contour level. The variation of Lx_{uu}/d with x/d is almost linear, mimicking the streamwise growth of the jet. The profiles somewhat segregate into two distinct groups of slope

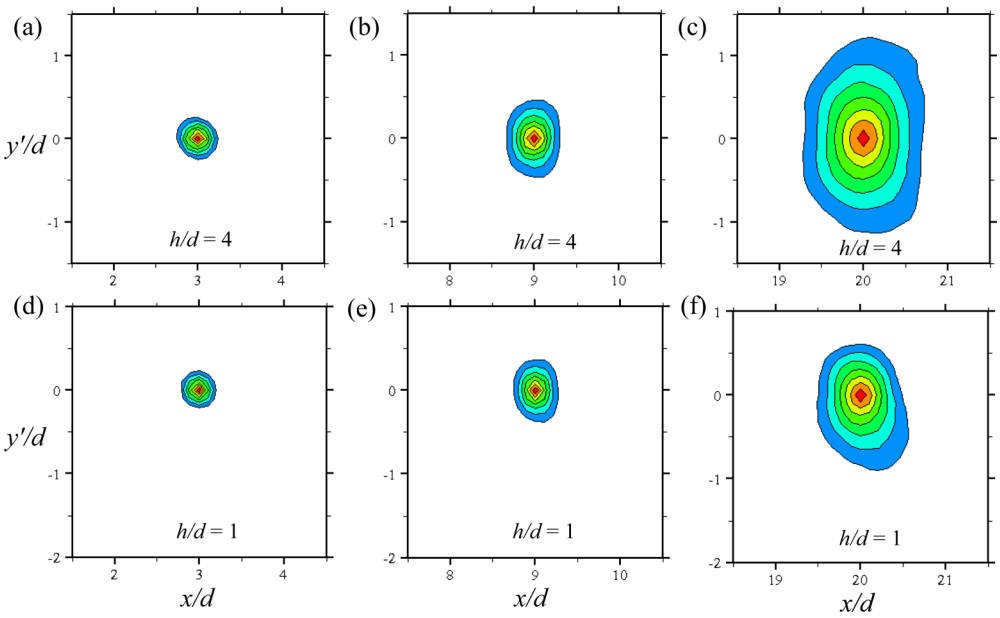

FIG. 17. Streamwise evolution of the surface-normal velocity fluctuation autocorrelation function R_{vv} at the jet centerline: (a) R_{vv} contours at $x/d = 3$ for $h/d = 4$, (b) R_{vv} contours at $x/d = 9$ for $h/d = 4$, (c) R_{vv} contours at $x/d = 20$ for $h/d = 4$, (d) R_{vv} contours at $x/d = 3$ for $h/d = 1$, (e) R_{vv} contours at $x/d = 9$ for $h/d = 1$, and (f) R_{vv} contours at $x/d = 20$ for $h/d = 1$. Contour levels are from 0.3 to 0.9 at intervals of 0.1.

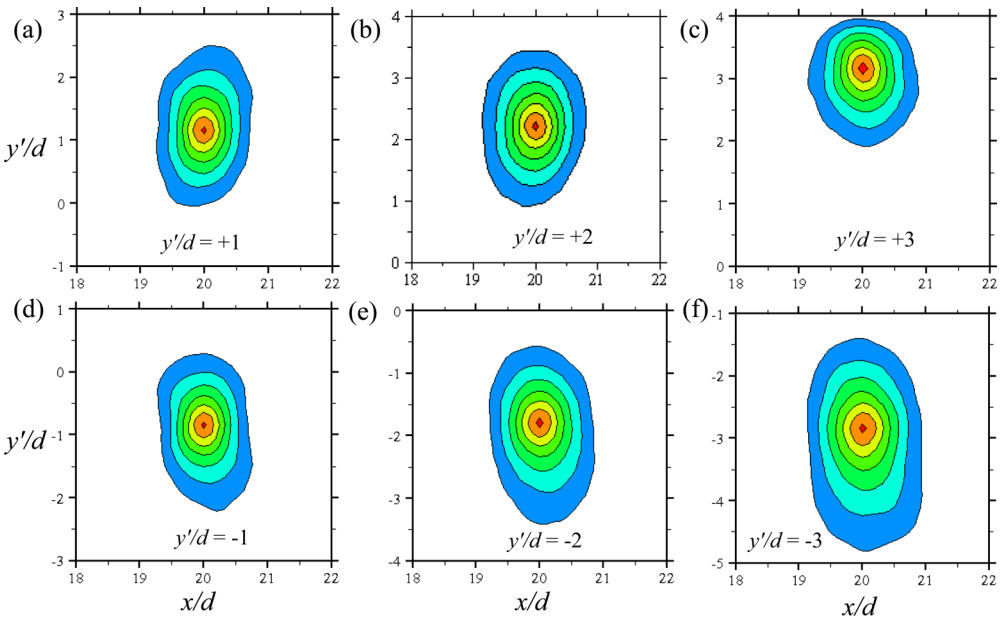

FIG. 18. Variation of the surface-normal velocity fluctuation autocorrelation function R_{vv} within upper and lower shear layers for the $h/d = 4$ jet at $x/d = 20$: (a) R_{vv} contours at $y'/d = 1$, (b) R_{vv} contours at $y'/d = 2$, (c) R_{vv} contours at $y'/d = 3$, (d) R_{vv} contours at $y'/d = -1$, (e) R_{vv} contours at $y'/d = -2$, and (f) R_{vv} contours at $y'/d = -3$. Contour levels are from 0.3 to 0.9 at intervals of 0.1.

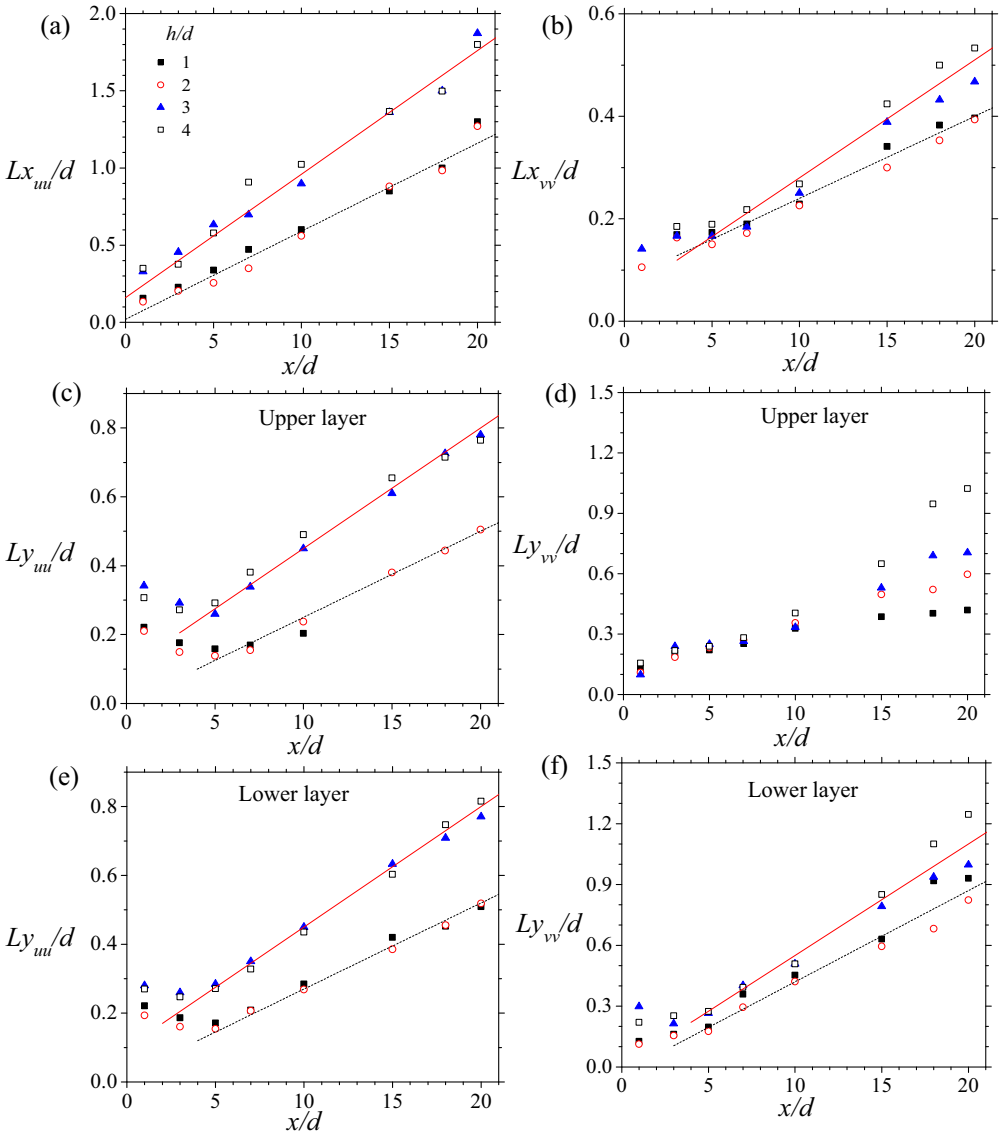

FIG. 19. Variation of the integral scales of the autocorrelation functions with streamwise distance x/d: (a) streamwise integral scale of R_{uu} at the jet centerline, (b) streamwise integral scale of R_{vv} at the jet centerline, (c) surface-normal integral scale of R_{uu} in the upper shear layer, (d) surface-normal integral scale of R_{vv} in the upper shear layer, (e) surface-normal integral scale of R_{uu} in the lower shear layer, and (f) surface-normal integral scale of R_{vv} in the lower shear layer.

0.057 ($h/d = 1$ and 2) and 0.080 ($h/d = 3$ and 4). These values were found to be in good agreement with the slopes measured for the Taylor microscale and Kolmogorov length scale distributions (not shown) in the far field of the jet. Figure 19(b) shows the streamwise evolution of the streamwise extent Lx_{vv} of R_{vv}. For R_{vv} the streamwise extent is defined as the streamwise distance between the self-correlation peak and downstream locations on the $R_{vv} = 0.3$ contour level. These also show an approximately linear growth with x/d, but the slopes are reduced to about 0.016 and 0.023 for the two groups. The surface-normal extent of R_{uu} measured from the self-correlation peak to the farthest

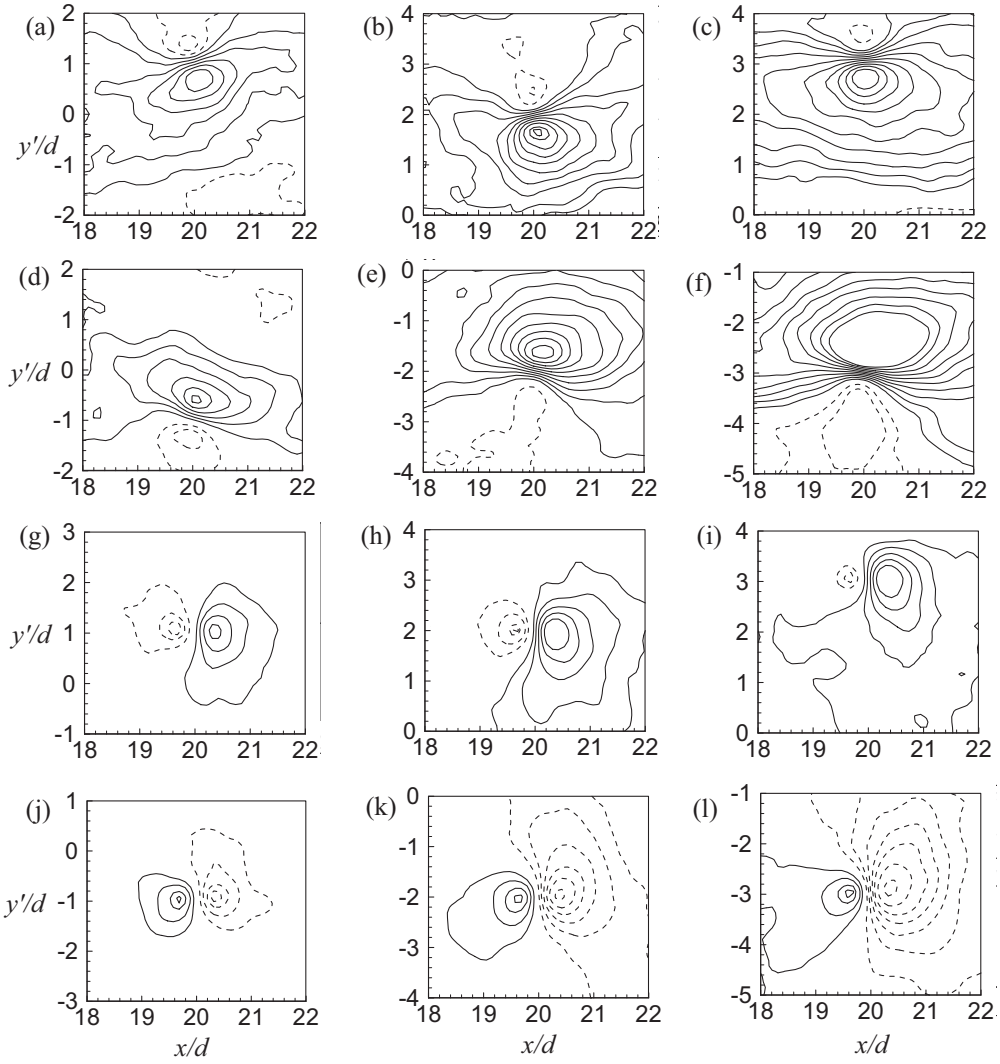

FIG. 20. Variation of the velocity fluctuation–swirling strength two-point correlation functions $R_{\lambda u}$ and $R_{\lambda v}$ within upper and lower shear layers for the $h/d = 4$ jet at $x/d = 20$: (a) $R_{\lambda u}$ at $y'/d = 1$, (b) $R_{\lambda u}$ at $y'/d = 2$, (c) $R_{\lambda u}$ at $y'/d = 3$, (d) $R_{\lambda u}$ at $y'/d = -1$, (e) $R_{\lambda u}$ at $y'/d = -2$, (f) $R_{\lambda u}$ at $y'/d = -3$, (g) $R_{\lambda v}$ at $y'/d = 1$, (h) $R_{\lambda v}$ at $y'/d = 2$, (i) $R_{\lambda v}$ at $y'/d = 3$, (j) $R_{\lambda v}$ at $y'/d = -1$, (k) $R_{\lambda v}$ at $y'/d = -2$, and (l) $R_{\lambda v}$ at $y'/d = -3$. Contour levels vary from -0.04 to 0.2 at intervals of 0.02.

location on the $R_{uu} = 0.3$ contour level in the upper shear layer are plotted in Fig. 19(c). The profiles indicate an initial decline in the Ly_{uu}/d after which it increases monotonically. For $x/d \geqslant 5$, the profiles approximately follow straight lines of slope 0.025 and 0.035. The corresponding profiles for R_{vv} (Ly_{vv}/d) are shown in Fig. 19(d). Here correlations grow almost linearly and at the same rate for $x/d < 10$. In the interaction region, the damping influence of the free surface leads to reductions in slope by amounts that increase with decreasing offset height ratio. The surface-normal extent of R_{uu} measured from the self-correlation peak to the farthest location on the $R_{uu} = 0.3$ contour level in the lower shear layer are depicted in Fig. 19(e). These are similar to those measured in the upper shear layer, indicating a nearly uniform outward growth of streamwise correlations. The variation of the surface-normal extent of R_{vv} in the lower shear layer is shown in Fig. 19(f). The values of

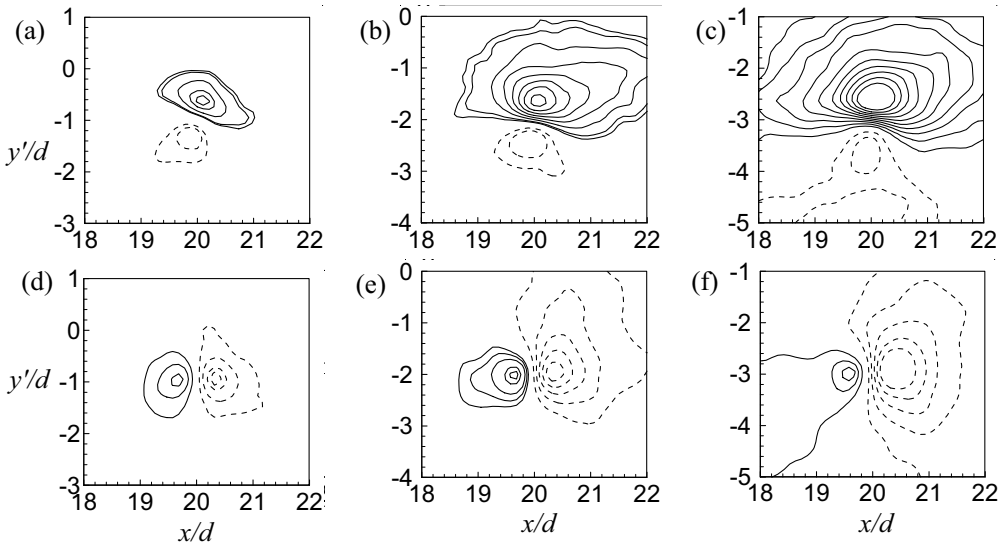

FIG. 21. Variation of the velocity fluctuation–swirling strength two-point correlation functions $R_{\lambda u}$ and $R_{\lambda v}$ within the lower shear layer for the $h/d = 1$ jet at $x/d = 20$: (a) $R_{\lambda u}$ at $y'/d = -1$, (b) $R_{\lambda u}$ at $y'/d = -2$, (c) $R_{\lambda u}$ at $y'/d = -3$, (d) $R_{\lambda v}$ at $y'/d = -1$, (e) $R_{\lambda v}$ at $y'/d = -2$, and (f) $R_{\lambda v}$ at $y'/d = -3$. Contour levels vary from -0.04 to 0.2 at intervals of 0.02.

Ly_{vv}/d follow an approximately linear profile of slope 0.055 for $h/d = 3$ and 4, which decreases to approximately 0.045 for $h/d = 1$ and 2 for $x/d \leqslant 15$. Beyond $x/d \approx 15$, the profiles exhibit a significant departure from a straight line, which is in concert with the strong impact of the jet confinement on the surface-normal velocity fluctuations.

3. Two-point correlations between the velocity fluctuations and swirling strength

To investigate the relationship between the spanwise vortices identified in the instantaneous visualizations and the velocity fluctuations, the two-point correlation between velocity fluctuations and swirling strength can be used. These correlations are dynamically significant in the sense that they provide an indication of the average spatial extent and strength of the velocity fields associated with the vortices in the jet. These vortices were identified to be predominantly retrograde vortex cores in the upper shear layer and prograde vortex cores in the lower shear layer. The values of the swirling strength $\lambda_{ci,z}$ were calculated using the two-dimensional approximation [34].

Figure 20 shows the isocontours of the two-point correlation between the velocity fluctuations and swirling strength ($R_{\lambda u}$ and $R_{\lambda v}$) at the various surface-normal locations for the $h/d = 4$ jet at $x/d = 20$. The isocontours of $R_{\lambda u}$ for reference locations in the upper shear layer are presented in Figs. 20(a)–20(c). For each of these cases, a retrograde vortex core is detected at the reference location, as identified by negative $R_{\lambda u}$ above the reference location and positive $R_{\lambda u}$ beneath it. At $y'/d = 1$, a secondary negative $R_{\lambda u}$ appears in the lower shear layer, which implies that the correlation at this reference location captures the spanwise vortex cores in both halves of the shear layer. At this location, the contours show an inclination angle of approximately 75° with respect to the upstream direction. As the reference location approaches the free surface, the positive correlations are intensified, while the negative correlations are suppressed, with the inclination angle increasing from 75° to approximately 86° at $y'/d = 3$. The contours of $R_{\lambda u}$ for reference locations in the lower shear layer are presented in Figs. 20(d)–20(f). In the lower shear layer, $R_{\lambda u}$ is positive above the reference location and negative below the reference location, indicating the presence of a prograde vortex core at the reference location. The correlations are enhanced with increasing distance from

$y'/d = 0$, but the streamwise inclination angle remains relatively constant at approximately 78°. Figures 20(g)–20(i) show the contours of the $R_{\lambda v}$ correlations in the upper shear layer: $R_{\lambda v}$ is negative upstream of the reference location and positive downstream of the reference location, indicating the flow around a retrograde vortex. Moving closer to the free surface leads to damping of the negative correlations and enhancement of the positive correlations. The streamwise inclination angles at $y'/d = 1,2$, and 3 are 7.6°,7°, and 3.2°, respectively, indicating a modest reduction in the streamwise inclination angle of the $R_{\lambda v}$ correlation. In the lower shear layer [Figs. 20(j)–20(l)], $R_{\lambda v}$ is positive upstream and negative downstream of the reference location, as expected for the prograde vortex at this location. At larger distances from $y'/d = 0$, enhancements are observed while the angle of inclination remains relatively constant at approximately 7° with respect to the downstream direction.

Figure 21 shows the velocity fluctuation–swirling strength correlation functions $R_{\lambda u}$ and $R_{\lambda v}$ at $x/d = 20$ for $h/d = 1$ in the lower shear layer. Due to the increased confinement, both correlation levels are smaller when compared to those of $h/d = 4$. Nevertheless, the streamwise inclination angles for $R_{\lambda u}$ and $R_{\lambda v}$ are approximately 77° and 6°, which are in good agreement with those observed for the $h/d = 4$ jet.

IV. CONCLUSION

An experimental investigation has been conducted to characterize the interaction between the free surface and a submerged square jet at a low Reynolds number (Re = 5500). A particle image velocimetry system was used to perform the velocity measurements in the vertical symmetry plane of the jet. Four offset height ratios of approximately $h/d = 1,2,3$, and 4 were considered in order to quantify the influence of jet confinement on the flow characteristics.

Instantaneous visualizations of the flow revealed the jet structure as comprising counterrotating spanwise vortex cores and braidlike structures propagating in the streamwise direction. The visualization results indicate that the effect of jet confinement is to cancel the turbulent-nonturbulent interface and suppress the vortical structures in the upper shear layer.

Contours of the mean streamwise velocity, Reynolds shear stress, and mean spanwise vorticity indicate that the effect of confinement is to reduce the Reynolds shear stress, mean spanwise vorticity, and growth of the jet in the upper shear layer relative to the lower shear layer. Confinement effects were also observed in the maximum mean streamwise velocity decay and the turbulence intensities measured at the centerline. The velocity scale $U_j d/h$, which accounts for changes in the offset height ratio, collapses the maximum mean velocity decay and surface velocity defect profiles fairly well in the interaction region. The surface velocity measurements indicate that the free surface is in a state of strain due to the alternating acceleration and deceleration of the surface current. The straining effect is more dramatic as the offset height ratio is reduced. The surface turbulence intensities indicate a general enhancement with increasing offset height ratio, but the confinement leads to a dramatic reduction in surface-normal turbulence intensity levels within the interaction region. This reduction is due to the damping effect of the free surface on the surface-normal fluctuations and is an indication of the redistribution of the turbulent kinetic energy from the surface-normal velocity fluctuations to the streamwise velocity fluctuations.

The effects of the jet offset height ratio on the turbulence structures were characterized using the joint probability density function between the velocity fluctuations and two-point correlations. The joint probability density function increases with the streamwise growth of the jet, but decreases in the direction away from the jet centerline. At a given streamwise location, reducing the jet offset height ratio produces a commensurate reduction in the joint probability density function due to the increased confinement by the free surface. These observations were supported by the weighted joint probability density function distributions. The two-point correlation functions of the streamwise and surface-normal velocity fluctuations also grow with downstream distance, but less rapidly with decreasing offset height ratio. For the streamwise velocity fluctuation, the correlation function is augmented in both halves of the shear layer. On the contrary, the damping effect of

the free surface on the surface-normal velocity fluctuations suppresses the surface-normal velocity fluctuation autocorrelation function in the upper shear layer. This is also consistent with the turbulent kinetic energy redistribution from the surface-normal velocity fluctuations to the streamwise velocity fluctuations near the free surface. The two-point velocity correlation results are complemented by the two-point correlation functions of the velocity fluctuations and the swirling strength. The velocity–swirling strength two-point correlations support the damping effect of the free surface on the vortical structures in the upper shear layer and exhibit average streamwise inclinations that increase with distance towards the free surface.

ACKNOWLEDGMENT

The authors gratefully acknowledge the support of this work by research grants from the Natural Sciences and Engineering Research Council of Canada.

[1] L. J. S. Bradbury, The structure of a self-preserving turbulent plane jet, J. Fluid Mech. **23**, 31 (1965).
[2] I. Wygnanski and H. Fiedler, Some measurements in the self-preserving jet, J. Fluid Mech. **38**, 577 (1969).
[3] S. C. Crow and F. H. Champagne, Orderly structure in jet turbulence, J. Fluid Mech. **48**, 547 (1971).
[4] A. K. M. F. Hussain, Coherent structures—Reality and myth, Phys. Fluids **26**, 2816 (1983).
[5] H. J. Hussein, S. P. Capp, and W. K. George, Velocity measurements in a high-Reynolds-number, momentum-conserving, axisymmetric, turbulent jet, J. Fluid Mech. **258**, 31 (1994).
[6] F. F. Grinstein, E. Gutmark, and T. Parr, Near field dynamics of subsonic free square jets. A computational and experimental study, Phys. Fluids **7**, 1483 (1995).
[7] A. Abdel-Rahman, A review of effects of initial and boundary conditions on turbulent jets, WSEAS Trans. Fluid Mech. **5**, 257 (2010).
[8] C. G. Ball, H. Fellouah, and A. Pollard, The flow field in turbulent round free jets, Prog. Aerosp. Sci. **50**, 1 (2012).
[9] A. Dewan, M. Pathak, and A. K. Dass, A survey of selected literature on important flow properties and computational fluid dynamics treatments of incompressible turbulent plane and round jets in quiescent ambient, Indian J. Eng. Mater. Sci. **13**, 180 (2006).
[10] A. Roshko, Experiments on the flow past a circular cylinder at very high Reynolds number, J. Fluid Mech. **10**, 345 (1961).
[11] E. Gutmark, K. C. Schadow, T. P. Parr, D. M. Hanson-Parr, and K. J. Wilson, Noncircular jets in combustion systems, Exp. Fluids **7**, 248 (1989).
[12] N. Rajaratnam and J. A. Humphries, Turbulent non-buoyant surface jets, J. Hydraulic Res. **22**, 103 (1984).
[13] S. A. Ead and N. Rajaratnam, Plane turbulent surface jets in shallow tailwater, J. Fluid Eng. **123**, 121 (2001).
[14] T. F. Swean, S. E. Ramberg, M. W. Plesnia, and M. B. Stewart, Turbulent surface jet in a channel of limited depth, J. Hydraulic Eng. **115**, 1587 (1989).
[15] C. K. Madnia and L. P. Bernal, Interaction of a turbulent round jet with the free surface, J. Fluid Mech. **261**, 305 (1994).
[16] D. G. Anthony and W. W. Willmarth, Turbulence measurements in a round jet near a free surface, J. Fluid Mech. **243**, 699 (1992).
[17] D. T. Walker, C.-Y. Chen, and W. W. Willmarth, Turbulent structure in free-surface jet flows, J. Fluid Mech. **291**, 223 (1995).
[18] G. Sankar, R. Balachandar, and R. Carriveau, Tailwater effects on the characteristics of a square jet near a free-surface, J. Hydraulic Res. **46**, 504 (2008).
[19] M. S. Rahman and M. F. Tachie, in *Turbulence, Heat and Mass Transfer*, edited by K. Hanjalic, T. Miyauchi, D. Borello, M. Hadzabdic, and P. Venturini (Begell House, New York, 2015), Vol. 8, p. 361.
[20] J. Tian, V. Roussinova, and R. Balachandar, Characteristics of a jet in the vicinity of a free surface, J. Fluid Eng. **134**, 031204 (2012).

[21] H. Tsunoda, Y. Shimizu, and T. Kashiwagi, Plane offset jet discharged into water of finite depth, JSME Int. J. B **49**, 1111 (2006).
[22] M. Raffel, C. E. Willert, and J. Kompenhans, *Particle Image Velocimetry: A Particle Guide* (Springer, New York, 1998).
[23] H. W. Coleman and W. G. Steele, Engineering applications of experimental uncertainty analysis, AIAA J. **33**, 1888 (1995).
[24] P. E. Dimotakis, R. C. Miake-Lye, and D. A. Papantoniou, Structure and dynamics of round turbulent jets, Phys. Fluids **26**, 3185 (1983).
[25] J. Westerweel, T. Hofmann, C. Fukushima, and J. C. R. Hunt, The turbulent/non-turbulent interface at the outer boundary of a self-similar turbulent jet, Exp. Fluids **33**, 873 (2002).
[26] C. B. da Silva and J. C. F. Pereira, Invariants of the velocity-gradient, rate-of-strain, and rate-of-rotation tensors across the turbulent/nonturbulent interface in jets, Phys. Fluids **20**, 055101 (2008).
[27] J. Philip and I. Marusic, Large-scale eddies and their role in entrainment in turbulent jets and wakes, Phys. Fluids **24**, 055108 (2012).
[28] J. Mi and G. J. Nathan, Statistical properties of turbulent free jets issuing from nine differently-shaped nozzles, Flow Turbul. Combust. **84**, 583 (2010).
[29] W. R. Quinn and J. Militzer, Experimental and numerical study of a turbulent free square jet, Phys. Fluids **31**, 1017 (1988).
[30] N. T. Obot, M. L. Graska, and T. A. Trabold, The near field behaviour of round jets at moderate Reynolds numbers, Can. J. Chem. Eng. **62**, 587 (1984).
[31] J. Wallace and R. Brodkey, Reynolds stress and joint probability density distributions in the u-v plane of a turbulent channel flow, Phys. Fluids **20**, 351 (1977).
[32] M. Agelinchaab and M. F. Tachie, Characteristics and structure of turbulent 3D offset jets, Int. J. Heat Fluid Flow **32**, 608 (2011).
[33] R. J. Volino, M. P. Schultz, and K. A. Flack, Turbulence structure in a boundary layer with two-dimensional roughness, J. Fluid Mech. **635**, 75 (2009).
[34] N. Hutchins, W. T. Hambleton, and I. Marusic, Inclined cross-stream stereo particle image velocimetry measurements in turbulent boundary layers, J. Fluid Mech. **541**, 21 (2005).